Soils and Rocks
An International Journal of Geotechnical and Geoenvironmental Engineering
www.soilsandrocks.com
ISSN 1980-9743
ISSN-e 2675-5475

Advancing transportation geotechnics through digital technologies

António Gomes Correia[1#], Mohammad Jawed Roshan[1],
Ionut Dragos Moldovan[2,3], Joaquim Tinoco[1], Dominic Owusu-Ansah[1],
Sinem Tola[1], Manuel Parente[1], Miguel Azenha[1]

Article

Keywords
Digital technologies
Self-sensing geomaterials
Bender element
Remote sensing
Building information modelling
Artificial intelligence

Abstract

The integration of advanced digital technologies is revolutionizing transportation geotechnics, enabling unprecedented achievements in efficiency of design, construction and maintenance contributing to more sustainable infrastructure developments. This paper explores cutting-edge advancements in self-sensing geomaterials, stiffness characterization using bender elements in unbound geomaterials, remote sensing, bridge scour detection and building information modelling (BIM), showcasing their transformative potential. Self-sensing geomaterials embedded with nanomaterials act as sensors provide real-time stress, strain and loading monitoring, enhancing health structural monitoring. Stiffness characterization is upscaled from sand to unbound aggregates through the application of bender element testing. Remote sensing technologies, including InSAR, enable slope stability assessments across networks, while AI-powered predictive models improve landslide risk mitigation, as well as network-scale bridge scour detection. The paper also highlights the BIM's contribution to infrastructure sustainable practices through the use of recycled construction and demolition wastes (RCDWs).

1. Introduction

The advancements in digital technologies have significantly revolutionized various sectors, including transportation geotechnics, across the globe. These advancements encompass a wide range of tools, methodologies, and materials, including sensors, data acquisition systems, remote sensing technologies, Building Information Modeling (BIM), and data fusion using artificial intelligence (AI) and machine learning (ML). Integrating these digital technologies into transportation geotechnics improves project efficiency, design, construction through real-time monitoring, enhanced data accuracy, and predictive maintenance strategies, leading to more informed decision-making throughout the project lifecycle (Gomes Correia & Gastine, 2024).

This study collectively discusses advancements such as self-sensing geomaterials, remote sensing, bridge scouring, and BIM, based on research conducted by the authors under various research projects. The self-sensing cementitious geomaterial was developed under the In2Track2 (European Comission, 2021) and In2Track3 (European Comission, 2023) projects, funded by the European Union, at the Institute for Sustainability and Innovation in Structural Engineering (ISISE) of the University of Minho. The automatic bender element sensor, developed under the CEN-DynaGeo project (CEN-DynaGEO, 2022), was developed through collaboration between ISISE at the University of Minho and Civil engineering research and innovation for sustainability (CERIS) at Instituto Superior Técnico, University of Lisbon. Additionally, bender element field sensors were developed under the INTENT project (Universidade Lusófona, 2023) at ISISE, University of Minho, in collaboration with CERIS at Instituto Superior Técnico, University of Lisbon, and Lusófona University. In addition, the topic related to BIM is connected to the RecycleBIM project at ISISE, University of Minho (2022).

Concerning the self-sensing geomaterials, they can be categorized as either bulk or localized. technologies such as distributed fiber optic sensors, self-sensing geosynthetics, and self-sensing materials provide bulk monitoring, while spot sensors offer localized monitoring (Roshan et al., 2025). In geotechnical engineering, various sensors are employed

#Corresponding author. E-mail address: agc@civil.uminho.pt
[1]Universidade do Minho, Instituto para a Sustentabilidade e Inovação em Estruturas de Engenharia, Departamento de Engenharia Civil, Laboratório Associado de Produção Avançada e Sistemas Inteligentes, Guimarães, Portugal.
[2]Universidade Lusófona, Faculdade de Engenharia, Lisboa, Portugal.
[3]Universidade de Lisboa, Instituto Superior Técnico, Centro de Investigação e Inovação em Engenharia Civil para a Sustentabilidade, Lisboa, Portugal.

Submitted on May 4, 2025; Final Acceptance on June 4, 2025; Discussion open until November 30, 2025.
Editor: Renato P. Cunha
https://doi.org/10.28927/SR.2025.007525

to monitor the behavior of geomaterials during both the construction stage and the operational service life (Hong et al., 2016). Among others, sensors such as piezometers (for measuring pore water pressure), thermistors and temperature sensors (for monitoring temperature variations), strain gauges and fiber optic sensors (for detecting deformation), inclinometers (for tracking lateral ground movement), load cells (for measuring applied loads), and pressure cells (for assessing induced stresses) are commonly used (Huang et al., 2012; Ha et al., 2018). However, external sensors attached to geomaterials in the field have several disadvantages, including complex installation procedures, localized and point-specific measurements, excessive congestion of sensors and cabling, susceptibility to environmental factors, the need for continuous monitoring and calibration, and the potential to cause localized degradation of the geomaterial during installation (Roshan et al., 2025). To address many of these challenges, self-sensing cementitious materials can be employed in transportation infrastructure systems (Roshan et al., 2024c). The self-sensing cementitious geocomposites, developed by integrating electrically conductive materials into conventional cement-stabilized geomaterials, show great promise (Roshan et al., 2024a). For instance, these innovative self-sensing cementitious materials can provide distributed sensing information rather than measurements at localized points, which is particularly important for linear projects such as roads and railways (Gomes Correia & Roshan, 2024). In addition, they can intrinsically function as sensors, eliminating the need for external devices (Huang et al., 2018). This enables real-time and remote monitoring, integrated functionality, and reduced future costs. These self-sensing cementitious composites can be used to measure moisture variations, temperature, strain and stress levels, as well as degradation and damage. For instance, Roshan et al., (2023) employed such geomaterials for automatic degradation and damage detection without requiring additional sensors. Their findings demonstrated a good correlation between electrical signals and Particle Image Velocimetry (PIV) results.

As referred, these self-sensing cementitious materials can be employed in both bulk form and sensor form. In bulk form, an entire layer of infrastructure is constructed using self-sensing cementitious materials. In sensor form, small-sized self-sensing cementitious sensors are embedded within the transportation infrastructure (Roshan et al., 2025). These composites have already been used in several pilot projects in the field, both as bulk self-sensing materials (e.g., Borke Birgin et al., 2022) and as small-sized sensors (e.g., Ding et al., 2022). However, several factors, such as moisture content, temperature, curing time, type and content of conductive fillers (e.g., carbon-based), dispersion quality, type of electrodes, and measurement systems, significantly affect their performance and require optimization and calibration prior to application (Roshan et al., 2024b). In this paper, the optimized self-sensing cementitious geocomposite, based on these factors, is discussed in terms of its effectiveness in degradation and damage detection.

Another very used sensor in geotechnical applications is wave-based sensor, such as bender elements, which is widely used in transportation infrastructure for geotechnical evaluation (Moldovan & Gomes Correia, 2017; Kang et al., 2021). However, issues such as the optimal spacing between transmitter and receiver elements, alignment, measurement systems, and signal interpretation must be addressed to ensure reliability. For example, Moldovan & Gomes Correia (2021) optimized the placement of receiver elements based on experimental and computational methods. Furthermore, GeoHyTE, a numerical software based on the hybrid Trefftz finite element method, was developed to automatically interpret shear wave and small-strain shear modulus data (Moldovan et al., 2024). Other studies have employed lateral dissipation boundaries to enhance the efficiency of bender element testing by reducing interference between shear and compressive waves (Moldovan et al., 2025). In this paper, following the initial developments for sand (Moldovan & Gomes Correia, 2021), preliminary results are presented demonstrating the feasibility of designing an upscaled bender element system for unbound granular material. The developed upscaled equipment, equipped with different bender element configurations, is capable of testing UGM without downscaling the particle size distribution.

Another important issue in transportation geotechnics is the assessment of slope stability network conditions. For this purpose, remote sensing approaches, combining spaceborne and ground-based synthetic aperture radar (SAR), have markedly improved slope instability detection (Frodella et al., 2017; Di Traglia et al., 2018). However, their application is limited by several interrelated factors. In Frodella et al. (2017) and Di Traglia et al. (2018), ground-based SAR instruments are confined to slopes within their direct line of sight, creating blind areas where dense vegetation or seasonal snow obstructs the radar beam. The steep, mountainous terrain further exacerbates these challenges by inducing geometric distortions such as foreshortening and layover, which warp the true slope geometry and complicate precise displacement retrieval. Finally, because these studies are restricted to Italian Alpine settings, their workflows and model outputs have yet to be validated in regions with different lithological, climatic, or geomorphological characteristics. Collectively, these constraints leave critical gaps in our understanding of slope-failure mechanisms and hinder the development of universally effective predictive models.

Accurate prediction of such events is particularly relevant for transportation infrastructure managers tasked with monitoring vast networks of slopes. In this context, remote sensing techniques, especially those using satellite data, have proven to be effective tools for assessing and tracking slope stability (Nhu et al., 2020). In their study of the Cameron Highlands, Malaysia, Nhu et al. (2020) combined InSAR, high-resolution imagery, and field surveys to identify 152 landslide sites and generated susceptibility maps using Logistic Regression, Logistic Model Tree, and Random Forest, achieving area under curve (AUC) values of 0.92, 0.90, and 0.88, respectively. However, the work is constrained by a relatively small, geographically confined dataset that limits generalizability; it relies exclusively on static conditioning factors, omitting dynamic triggers such as rainfall intensity and groundwater fluctuations. Moreover, it shows minimal performance differences among the three algorithms, suggesting that data quality and feature engineering may be more important than model choice. It also faces remote-sensing challenges in tropical mountainous environments, where dense vegetation and frequent cloud cover can impede landslide detection and validation. These limitations highlight the need for larger, more diverse datasets, the inclusion of time-varying environmental variables, and hybrid modeling approaches to develop effective, transferable predictive frameworks for early warning and risk assessment. To address this gap at the network scale, this study proposes a machine learning (ML)-based framework for predicting slope movements using vertical displacement time series derived from Interferometric Synthetic Aperture Radar (InSAR) data. The main goal is to optimize these models for improved prediction accuracy. By combining satellite imagery with AI-driven approaches, this work seeks to enhance automated slope monitoring and support data-informed decision-making in instability risk management, contributing to the broader goal of disaster risk reduction.

Among other transportation infrastructures, bridges are also key elements, enabling the movement and operation of vehicles over obstacles such as valleys and rivers. In bridges constructed over rivers, scour around the foundation caused by flowing water is one of the major challenges (Bao et al., 2017). The reduced support of the bridge foundation caused by scour can eventually lead to failure and collapse. Therefore, early detection of scour and the implementation of countermeasures are crucial for the effective and continuous operation of transportation infrastructure without interruption (Selvakumaran et al., 2018). In addition to the installation of sensors on the bridges themselves and other wireless inspection methods, vehicle-assisted methods (e.g., train-based inspection) for bridge scour can be an effective approach (Fernandes et al., 2024). In the train-based method, sensors such as vibration and acceleration sensors are installed on trains to automatically record vibrations as the train passes over the bridge. The recorded vibrations can then be used for scour analysis, detection, and estimation (Hoang et al., 2018). Indeed, scour is the leading cause of bridge collapses, emphasizing the urgent need for effective scour detection methodologies. The 2015-2016 winter storms that affected a large area of England, Wales, Ireland, and Scotland are among the most recent incidents triggering floods (Barker et al., 2016). The precipitation levels that had been predicted were exceeded, and a series of storms began in November 2015, continuing until March 2016 (Marsh et al., 2016). In circumstances where the level of flooding was extreme, instances occurred of scouring at bridge infrastructures, which ultimately led to the structural collapse of bridges in certain instances (Standard, 2016). Barker et al. (2016) indicate that the loss of infrastructure, including roads and bridges, resulted in significant long-distance detours in specific regions, with complete repairs often requiring several months. Consequently, the immediate scour detection is very important. To do so, the dynamic response of the bridge can be assessed over time by processing the sensor data acquired by monitoring. Some of the most common techniques used to process acquired accelerations are Eigen frequency analysis (Prendergast et al., 2016), Continuous Wavelet Transformation (O'Brien et al., 2023), and Hilbert-Huang Transform (Lin & Chang, 2017). Many studies compare extracted parameters of damaged and healthy states of the bridges and use the difference to serve as a damage indicator (Elsaid & Seracino, 2014; Khan et al., 2021). The monitoring systems employed can be categorized into two distinct clusters. The direct monitoring method involves the collection of signals from sensors installed on the bridge structure. Conversely, the indirect method utilizes data acquired by sensors installed on vehicles crossing the bridge. This method does not result in service interruptions since the signals are acquired as the vehicle continues to travel (Tola et al., 2023a). Many studies have successfully detected damage using in-service acceleration signals (Prendergast et al., 2016; Zhang et al., 2023; McGeown et al., 2024; Shokravi et al., 2024). As Shokravi et al. (2024) demonstrate, long-term monitoring of a roadway bridge to detect damage is enabled by processing drive-by acceleration signals obtained from connected and autonomous vehicles. The methodology developed has not yet been applied to real-life applications, but has demonstrated considerable potential. A further study by McGeown et al. (2024) demonstrated the occurrence of bridge scour theoretically and experimentally by exhibiting the discrepancy between the indirect vehicle pitch signals of bridges in both damaged and healthy states. Machine Learning (ML) algorithms have also been incorporated into indirect monitoring studies for damage detection (Hajializadeh, 2022; Fernandes et al., 2024). In the study of Fernandes et al. (2024), bridge-crossing vehicles' accelerations are processed to extract the features that change in the presence of damage by an autoencoder to detect low-intensity scour damage. (Hajializadeh, 2022) adopted Convolutional Neural Networks (CNNs), which have been meticulously trained using a diverse set of vehicle accelerations from multiple crossings, encompassing varied travel speeds, noise levels, and rail irregularities.

The developed scour detection methodology presented here has three main contributions. Firstly, it verifies a previously proposed approach (Prendergast et al., 2016; Fitzgerald et al., 2019) through synthetic simulations and field-collected measurements (Tola et al., 2023b). Secondly, it introduces displacement-based analysis from onboard sensing to detect scour. Thirdly, it demonstrates a novel method for data acquisition, employing an innovative sensor unit mounted on in-service vehicles instead of relying on conventional track geometry cars. Extending the developed methodology to a network level involves utilizing machine learning (ML) models. Consequently, the necessity for establishing a numerical model for each bridge is rendered obsolete. Instead, an automated system can predict the presence and location of scour.

The last contribution in this paper is related with another critical consideration dealing with the coordination during the construction of transportation infrastructure. For this purpose, Building Information Modeling (BIM) plays a vital role in facilitating efficient collaboration among geotechnical engineers, structural engineers, and other stakeholders, thereby ensuring accurate project execution (Zhang et al., 2018). To develop an effective BIM model for transportation infrastructure, it is essential to integrate geotechnical data with data from other engineering disciplines (Tawelian & Mickovski, 2016).

In parallel, the construction industry is one of the largest contributors to environmental degradation worldwide. As a major consumer of natural resources and energy, it is responsible for significant pollution, depletion of materials, and greenhouse gas emissions (European Comission, 2020). Compounding this impact is the inefficiency with which resources are used—up to 85% of extracted materials are estimated to end up as waste (Pacheco-Torgal et al., 2020). A substantial share of this is construction and demolition waste (CDW), which accounts for 25-30% of the total waste produced in the EU. Fortunately, a large proportion of CDW (40-80%) consists of inert materials with high reuse potential, particularly in civil engineering applications (Han et al., 2021).

In geotechnical engineering, this shift toward circularity has created promising pathways for incorporating recycled materials into infrastructure. Recent studies have shown that granular waste from demolished structures—such as concrete, ceramics, and mixed aggregates—can be successfully used in applications such as subgrade layers, embankments, and backfill materials (Gomes Correia et al., 2025). These approaches reduce environmental impact while maintaining, or even enhancing, technical performance. Furthermore, they align with broader goals of sustainable development and resource efficiency. However, sustainability in geotechnics is not limited to material reuse. It increasingly relies on digital technologies that are reshaping how engineers design, build, monitor, and maintain geotechnical systems. Building Information Modeling (BIM), for example, is transforming construction workflows by acting as a digital twin of physical assets—capturing data on materials, geometry, and processes across a structure's lifecycle. When applied to the end-of-life phase of buildings, BIM enables precise inventories of reusable materials and facilitates more strategic planning for waste reduction and recycling (Nikmehr et al., 2021; Kang et al., 2022; Kuzminykh et al., 2024).

Together, these digital and data-driven approaches are ushering in a new era of intelligent geotechnical engineering, where sustainability goals are met not only through better material choices but also through smarter processes, predictive analytics, and automation. The convergence of circular economy principles, advanced sensing technologies, and integrated data platforms is creating unprecedented opportunities to reduce the environmental footprint of geotechnical works while improving resilience, safety, and cost-efficiency.

This paper explores how such innovations, spanning material reuse, digital twins, AI-driven monitoring, and automation, are collectively advancing the sustainable transformation of geotechnics. The scope of the work aims to illustrate how digitalization is enabling geotechnical engineering to meet the pressing challenges of climate change, resource scarcity, and infrastructure resilience.

2. Self-sensing geomaterials

In Structural Health Monitoring (SHM), sensors play a central role in collecting data related to the health condition of structures. To this end, the advancement of sensor technologies in transportation geotechnics is an important topic. In geotechnical engineering, sensors can be deployed in a distributed form (e.g., distributed fiber optics) or a spot form (e.g., pressure cells). Recently, in addition to these forms, the application of bulk sensing mechanisms, such as self-sensing cementitious composites, has also been investigated (Roshan & Gomes Correia, 2025). In addition, the bender element sensors can be deployed at a specific distance between the transmitter and receiver bender elements to record the stiffness of the geomaterial under traffic loading (Kang et al., 2023). Therefore, this section discusses self-sensing cementitious geocomposites and bender element sensors.

2.1 Self-sensing cementitious geocomposites

Self-sensing cementitious geocomposites are developed by incorporating electrically conductive materials into conventional cement-based materials. These conductive materials are typically categorized into two types: metal-based and carbon-based conductive fillers (Tian et al., 2024). While metal-based fillers can be used in fabricating self-sensing concrete pavements and other concrete structures, carbon-based conductive fillers are more commonly employed in the fabrication of self-sensing cementitious geocomposites.

Various carbon derivatives, such as carbon black (CB), carbon fibers (CF), graphite powders (GP), and carbon nanomaterials including carbon nanotubes (CNT) and carbon nanofibers (CNF), are widely used in these composites (Kang et al., 2024). The performance of self-sensing cementitious composites varies depending on the type and content of the conductive fillers. In general, the use of combined conductive fillers is a common approach to enhance the sensing efficiency of these materials.

Several factors influence the performance of self-sensing cementitious composites. These include the type and content of conductive fillers, their dispersion within the matrix, electrode materials and configurations, measurement systems, and external environmental factors such as moisture and temperature (Roshan et al., 2025). To fabricate effective self-sensing cementitious materials, optimizing the type and amount of conductive fillers is crucial.

The electrical resistance of cementitious composites generally decreases in three distinct stages as the content of conductive fillers increases, as illustrated in Figure 1 (Roshan et al., 2024a). In the first range (insulative phase), the reduction in electrical resistance is minimal, indicating insufficient filler content for effective self-sensing behavior. In this range, the conductivity mechanism is primarily based on ionic conduction, making the material highly sensitive to moisture variations. In the second range (percolation region), the conductivity is governed by both electron transport and partial ionic conduction. Here, the influence of moisture on electrical resistance becomes less significant, especially as the filler content approaches the end of the percolation threshold. In the third range (conductive phase), electron movement between conductive networks dominates the conductivity mechanism, and moisture has a negligible effect on electrical resistance. However, excessive use of conductive fillers is not recommended due to high costs and potential negative impacts on mechanical strength. Therefore, for optimal performance, conductive filler content should fall within the percolation threshold, achieving effective electrical conductivity while maintaining adequate mechanical strength.

To ensure effective electrical conductivity, uniform distribution of conductive fillers during fabrication is essential. However, the high surface area of carbon-based fillers often leads to agglomeration, resulting in non-uniform distribution and reduced conductivity. Thus, dispersion is a critical challenge in the fabrication of self-sensing cementitious materials. Various dispersion methods, including mechanical mixing, sonication, and chemical dispersion, are used to address this issue. A combination of these techniques is often recommended for achieving uniform distribution and optimal sensing performance.

In addition, other factors such as electrode materials and configurations, measurement systems, and environmental conditions (e.g., moisture and temperature) significantly affect the sensing performance. Detailed discussions on these aspects can be found in previous studies (Roshan et al., 2025; Roshan & Gomes Correia, 2025).

2.1.1 Application of self-sensing cement stabilized sand for sensing and degradation monitoring

The geomaterials used in transportation infrastructure are subjected to various types of loading, such as cyclic traffic loading, dynamic loading, vibration, and environmental effects (e.g., wetting–drying cycles and freezing–thawing cycles) throughout their service life (Roshan et al., 2022).

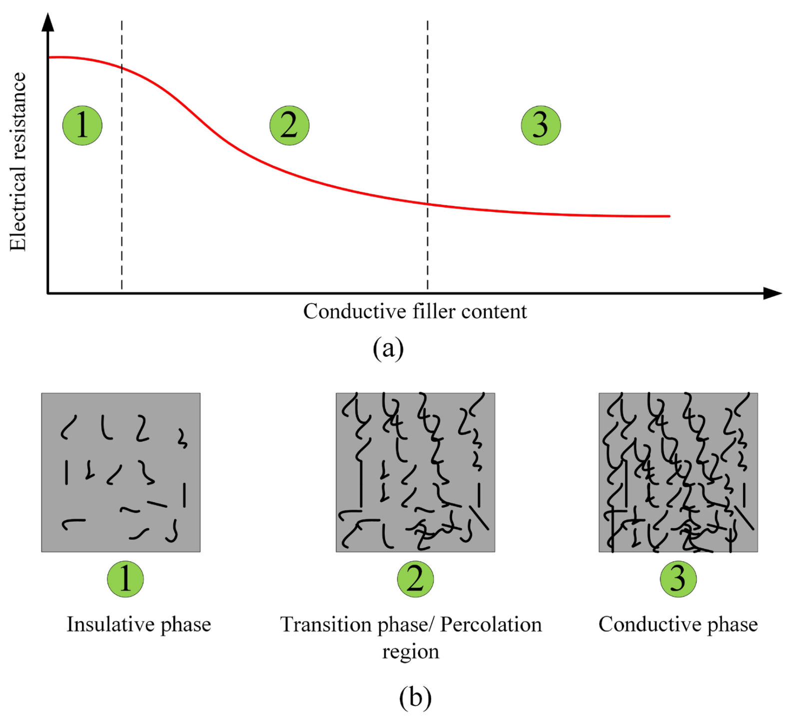

Figure 1. Influence of conductive fillers content on the electrical resistance of self-sensing cementitious materials with inclusion of carbon nanomaterials (CNM); (a) Correlation of electrical resistance – conductive filler content; (b) schematic illustration of conductive paths. Modified after Roshan et al. (2024a).

These conditions lead to degradation and damage, which can compromise the safety and reliability of transportation systems. To address these challenges, timely monitoring and detection of geomaterial condition is crucial.

In this regard, various types of sensors and technologies are employed for SHM of transportation infrastructure. Among these, self-sensing cementitious composites show great potential for traffic and degradation monitoring (Roshan & Gomes Correia, 2025). These materials are capable of detecting axle loads and material degradation without the need for external sensors. Additionally, they can be utilized for other applications, such as energy harvesting and ice or snow melting during cold seasons.

The self-sensing capability of these composites is primarily attributed to their piezoresistive properties, which enable the detection of traffic loads and structural degradation. Piezoresistivity refers to the change in electrical resistance caused by the alteration of conductive pathways under mechanical loading. A commonly used metric for analyzing electromechanical behavior is the Fractional Change in Resistance (*FCR*), defined by Equation 1:

$$FCR = \frac{\Delta R}{R_0} = \frac{R_i - R_0}{R_0} \tag{1}$$

where FCR stands for fractional changes in resistance, R_0 is the initial resistance, ΔR is the changes in resistance, and R_i is the resistance at certain loading level.

Figure 2 illustrates the results of electromechanical testing on 10% cement-stabilized sand doped with 3% of multi-walled carbon nanotubes (MWCNT) and graphene nanoplatelets (GNP) in equal proportions. Figure 2a presents the variation of *FCR* in response to cyclic compressive stress, ranging from low levels to the point of material failure. As shown in Figure 2a, *FCR* variation increases with increasing stress level. The pattern of *FCR* variation depends on the applied stress level. At low stress levels (up to 30.04% of ultimate strength), the *FCR* variation under cyclic loading is reversible. However, beyond this stress level, irreversibility in *FCR* begins to appear. For instance, at stress levels of 39.85% and 49.81% of the ultimate strength, the lower peaks of the *FCR* curves show signs of irreversibility. At higher stress levels, both lower peaks and upper baselines become irreversibly altered. Finally, after reaching the stress level at point 3 (89.66% of the ultimate strength), the direction of FCR variation reverses, as shown in Figure 2a. These changes in *FCR* patterns reflect varying degrees of material degradation and damage.

Figure 2b shows the correlation between *FCR* and the resilient modulus, calculated using Equation 2:

$$M_r = \frac{\sigma_d}{\varepsilon_r} \tag{2}$$

where M_r is resilient modulus, σ_d deviator stress, and ε_r is resilient strain.

The correlation between *FCR* and resilient modulus varies depending on the health condition of the self-sensing cementitious composite. At a cyclic stress level of 30% of ultimate strength, the *FCR* variation is reversible, and the resilient modulus increases significantly. However, beyond this point, *FCR* becomes increasingly irreversible, and the rate of increase in resilient modulus declines, especially after point 2, as shown in Figure 2b. These findings suggest that the relationship between *FCR* and resilient modulus can serve as a reliable indicator for tracking material degradation in self-sensing geomaterials. To further illustrate this behavior, Digital Image Correlation (DIC) results at points 1, 2, and 3 from Figure 2a are presented in Figure 2c. A comparison between Figures 2a and 2b with Figure 2c reveals that the degradation of the self-sensing cementitious sample increases with the applied stress level. For example, up to point 2, no visible cracks are observed in the DIC images. However, at point 3, a vertical crack can be observed at the center of the sample. The size of this crack increases further with rising stress levels. This comparison between Figures 2a and b with Figure 2c suggests that the variation in *FCR*, in relation to stress level and the corresponding resilient modulus, can effectively be used to monitor the degradation of self-sensing cementitious materials.

2.1.2 Application of self-sensing cementitious materials in the field

Self-sensing cementitious materials can be employed in two forms: bulk and sensor form. In the bulk form, a layer of self-sensing cementitious composite can be embedded into transportation infrastructure, with electrodes installed at specific locations. For example, these materials have been used in bulk form for snow and ice melting in transportation systems (Sassani et al., 2018). This feature is particularly effective and valuable for applications in cold regions.

One notable example is the use of a self-sensing pavement slab at Des Moines International Airport to mitigate ice formation (Sassani et al., 2018). The results revealed that the self-sensing pavement effectively melted snow and ice due to a power density of 300-350 W/m^2. Similar findings regarding the effectiveness of self-sensing pavement for snow and ice melting have been reported in other studies as well (e.g., Jiao et al., 2023). In addition to de-icing, self-sensing pavement has also been applied in bulk form for traffic detection. A road section equipped with self-sensing pavement was able to successfully detect vehicle axle loads (Borke Birgin et al., 2022).

On the other hand, in sensor form, self-sensing cementitious composites are produced in small sizes and function as intrinsic self-sensing sensors. These sensors have been successfully deployed in road (Han et al., 2009) and railway (Ding et al., 2022) applications for vehicle detection.

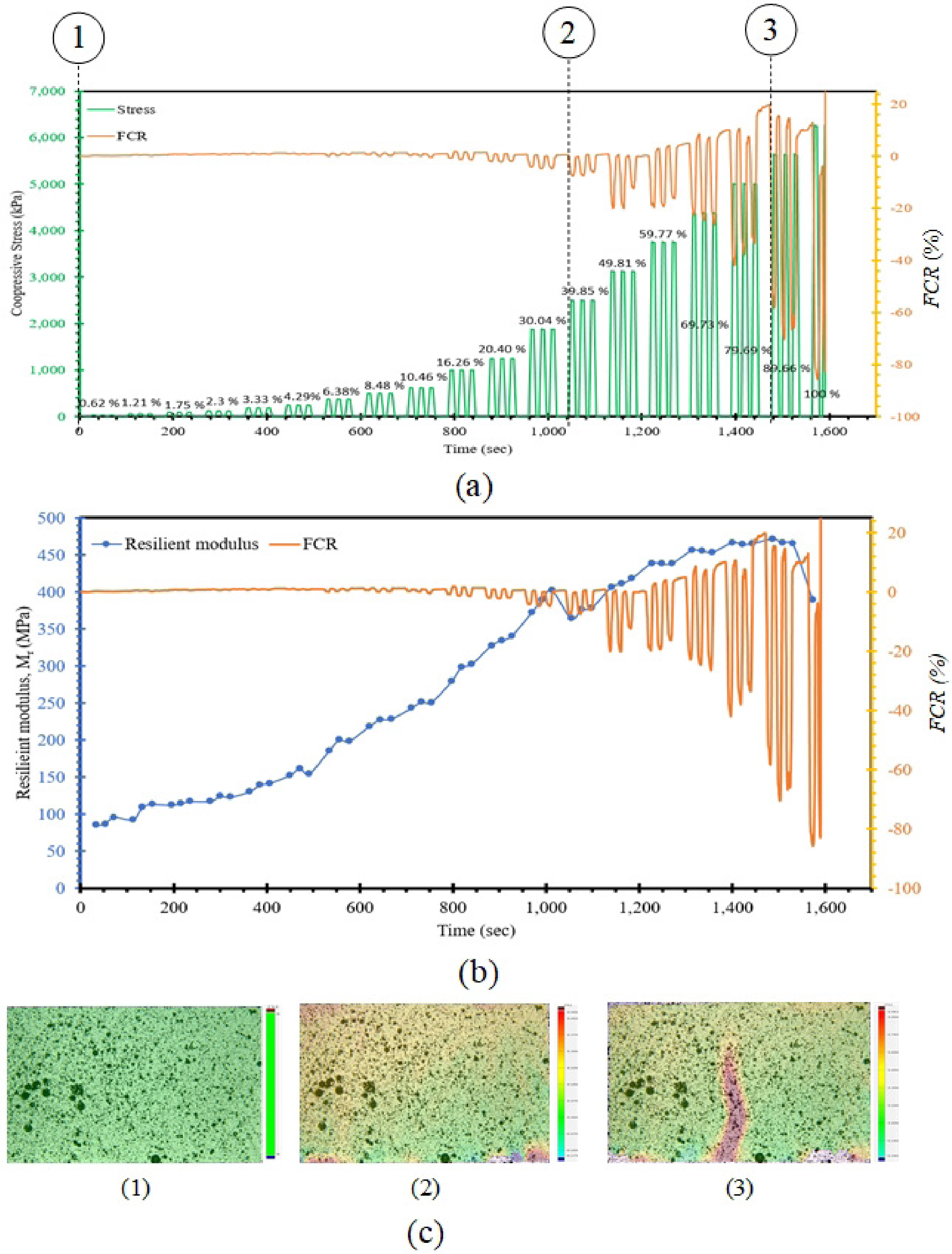

Figure 2. *FCR* variation under cyclic loading (a) Stress – *FCR* (b) Resilient modulus – *FCR* (c) Major strain based on DIC images at time instant of 1, 2, and 3 shown in Figure 2a. Modified after Roshan et al. (2023).

Although self-sensing cementitious materials demonstrate strong potential for field applications, their real-world use remains limited at this stage.

2.2 Bender elements as a self-sensing device

The bender element (BE) is a widely used sensor for measuring the small-strain shear modulus of geomaterials based on shear wave propagation (Viggiani & Atkinson, 1995). BE are themselves a type of self-sensing material. Indeed, they can be considered a self-sensing device when used properly, since the piezoelectric ceramic both actuates (generates waves) and senses (detects waves). Despite bender elements require external transducers to send/receive waves, as self-sensing materials they perform a similar function in assessing mechanical geomaterial response.

There is a potential in combining self-sensing materials with BE to develop embedded smart testing systems or even self-monitoring geostructures. To obtain the small-strain shear modulus, a transmitter bender element trigger a shear wave that propagates towards the receiver bender element. Although the shear wave travel time can be readily obtained from bender element signals, accurately identifying the shear wave arrival time remains a challenge due to signal irregularities, particularly the interference of compressive waves with the shear waves (Arulnathan et al., 1998; Lee & Santamarina, 2005). To address this challenge, the authors of this study have proposed several solutions. For instance, compressive wave interference can be reduced by optimizing the installation of bender elements so that the transmitter and receiver are in an eccentric configuration rather than a direct one (Moldovan & Gomes Correia, 2021). In another study, boundary dissipation layers were proposed to reduce the arrival of compressive waves at the receiver bender element (Moldovan et al., 2025). Additionally, a computational software called GeoHyte has been developed based on the hybrid Trefftz finite element method, to automatically update the small-strain shear modulus to optimize the correlation between the output signals obtained experimentally and numerically (Moldovan et al., 2024).

Although these previous studies have shown promising results, the tests were conducted only on sand, which consists of smaller particles compared to the unbound granular materials (UGMs) commonly used in transportation geotechnics, mainly in pavement and railway structural layers. To this end, a large-scale cylindrical chamber (30 cm in diameter and 60 cm in height) equipped with multiple bender elements was developed to analyze the performance of bender elements in UGMs. Figure 3 presents the details of the developed large-scale cylindrical chamber. As seen in Figure 3, the chamber is equipped with two bender elements at the pedestal and one bender element at the top cap. Due to the large distance between the transmitter and receiver bender elements, an amplification system was used to enhance the strength of the input signal. As seen in Figure 3, the UGM was compacted into the cylindrical chamber in dry conditions, with a density of 1889 kg/m^3. The void ratio of the compacted UGM in this study is 0.40. The initial findings regarding the influence of bender element configuration and echo measurement settings based on this chamber are discussed in this section.

2.2.1 Influence of bender element configuration

To evaluate the influence of bender element configuration on the output signals, the transmitter bender element was installed on the top cap of the cylindrical cell, while two receiver bender elements were installed at the pedestal of the cylindrical cell, as presented schematically in Figure 4. As shown in Figure 4, in one configuration, the receiver bender element is in a direct alignment with the transmitter, while in the other configuration, it is positioned eccentrically relative to the transmitter. In the direct configuration, the tip-to-tip distance between the transmitter and receiver bender elements is 560 mm, whereas in the eccentric configuration, the tip-to-tip distance is 565.28 mm, based on the Pythagorean theorem.

Figures 5 and 6 present the recorded output signals for the bender element configurations under direct transmission condition (red) and eccentric transmission condition (blue), across various input frequencies ranging from 200 Hz to 3 kHz. From these figures, it can be observed that the recorded

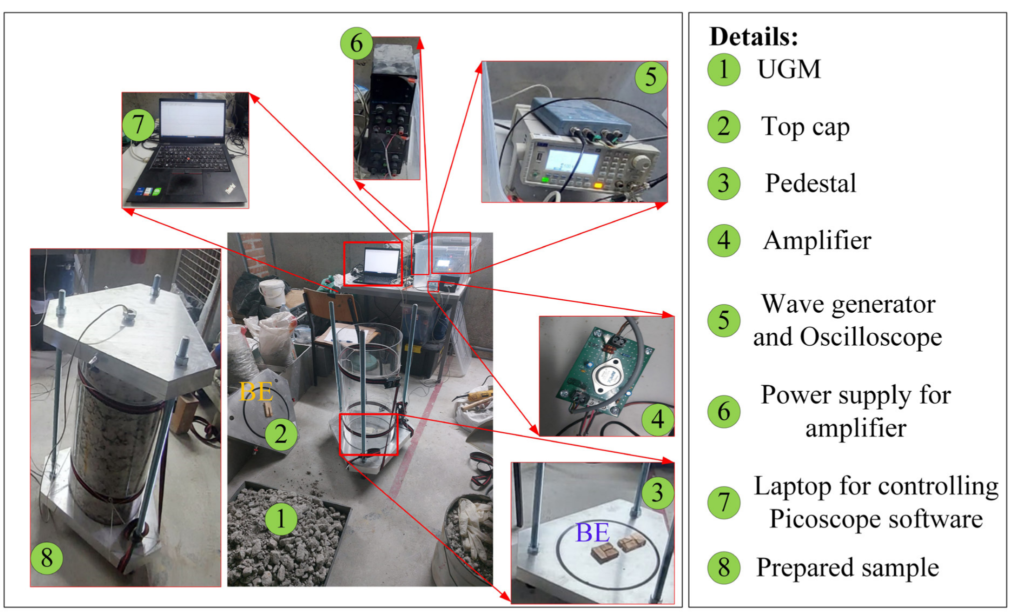

Figure 3. Details of large scaled cylindrical chamber.

signals differ depending on the configuration of the receiver bender element relative to the transmitter bender element.

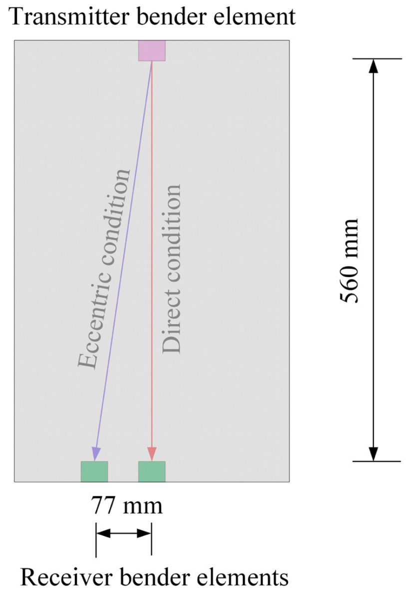

Figure 4. Configurations of receiver and transmitter bender elements (direct transmission and eccentric transmission).

The findings are consistent with a previous study conducted on sand (Moldovan & Gomes Correia, 2021).

Figure 5 illustrates the recorded shear wave signals under input frequencies ranging from 200 Hz to 700 Hz. As seen in the figure, the recorded signals vary in terms of waveform shape, clarity, and the level of interference between compressive (P) and shear (S) waves, depending on the receiver's configuration relative to the transmitter. In the direct configuration, the interference between shear and compressive waves is more prominent compared to the eccentric configuration. This interference can create challenges in signal interpretation, particularly in accurately identifying the shear wave arrival time for shear modulus measurement.

Compressive waves travel laterally and, after colliding with lateral boundaries, reflect back toward the receiver bender element. As a result, the eccentric receiver configuration tends to bypass much of the compressive wave energy, whereas most of the compressive wave is captured by the bender element aligned directly with the transmitter. Consequently, the signals recorded by the receiver in the eccentric configuration (Figure 5) exhibit a single, clearly defined peak, in contrast to the more complex waveform seen in the direct configuration. This makes identifying and selecting the shear wave arrival time more reliable and precise in the eccentric condition. However, it should also

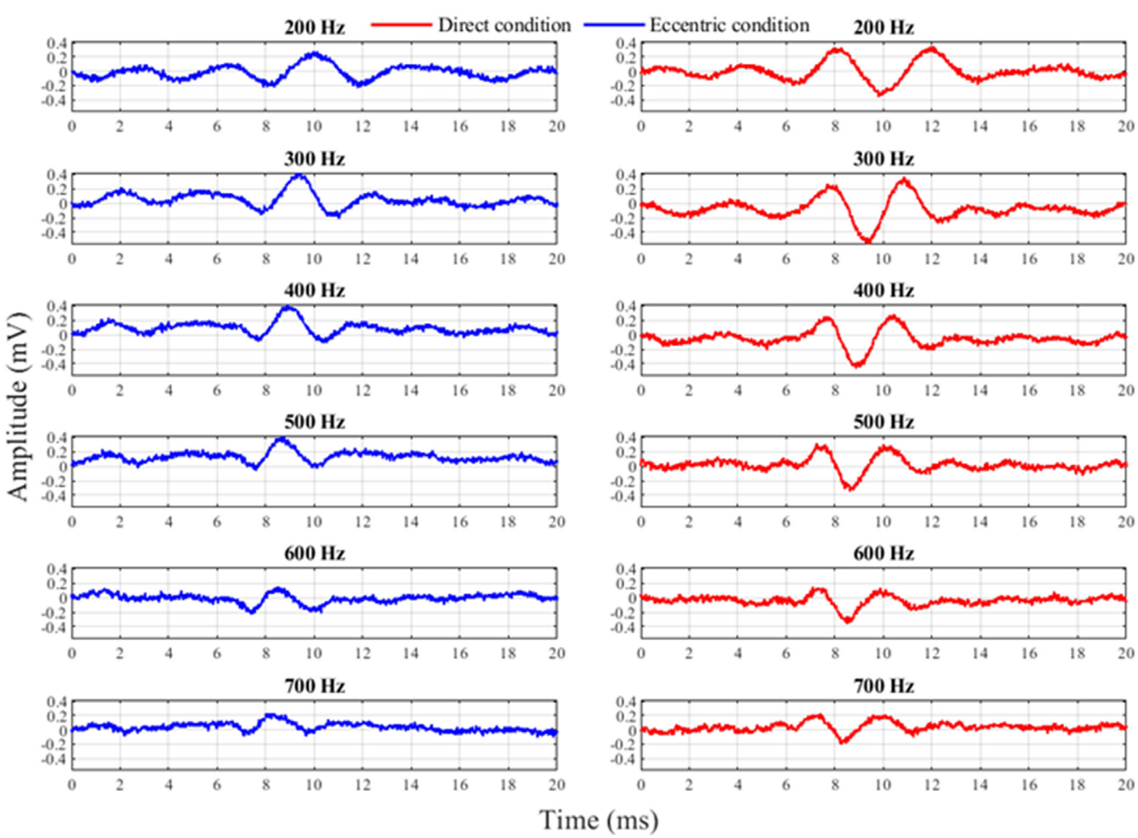

Figure 5. Output signals in eccentric transmission condition (blue color) and direct transmission condition (red color) for input frequencies ranging from 200Hz to 700 Hz.

be noted that signal attenuation in the eccentric configuration is greater compared to the direct configuration, as observed in Figure 5. In the eccentric setup, the shear wave travels a longer path than in the direct configuration, resulting in higher attenuation due to increased scattering at void spaces and particle interfaces. For this reason, the attenuation of output signals with increasing frequency is more pronounced in the eccentric configuration compared to the direct configuration.

Figure 6 illustrates the output signals under input frequencies ranging from 800 Hz to 3 kHz. This figure further confirms that the interference between compressive and shear waves in the direct condition is more significant compared to the eccentric condition. For instance, in the direct condition (red), the shear wave arrival peak completely disappears beyond the 1 kHz input frequency, and instead, compressive wave signals dominate at 2 kHz and 3 kHz. On the other hand, although the shear wave peak in the eccentric condition (blue) also disappears beyond 1 kHz, at input frequencies of 2 kHz and 3 kHz, the occurrence of compressive wave signal peaks is significantly lower compared to the direct condition. Therefore, it can be concluded that the interference of compressive waves with shear waves is greater in the direct condition than in the eccentric condition.

To illustrate the calculation of the shear modulus based on the results reported above, the case of a 700 Hz input frequency is considered. For this situation, Figure 7 presents the output signals obtained in direct and eccentric transmission conditions. Prior to the initial peak, considerable irregularities are present in the direct condition compared to the eccentric condition due to compressive wave interference, as seen in Figure 7. However, it should be noted that the behavior of geomaterials, particularly UGMs, is anisotropic, meaning the small-strain shear modulus can vary depending on the direction of wave propagation. Consequently, the calculated small-strain shear modulus in the direct condition can differ from that in the eccentric condition. For instance, Figure 7 presents the shear wave signals for both eccentric and direct conditions. Considering the travel lengths from Figure 4 and the travel times from Figure 7, the obtained small-strain shear modulus for the UGM sample compacted in a dry condition at a density of 1889 kg/m^3 is 16.51 MPa for the direct condition and 12.76 MPa for the eccentric condition.

UGM stiffness is both stress-dependent and fabric-dependent. However, in the present study, the tests were conducted under k_0 condition. Therefore, the higher shear modulus observed in the vertical direction configuration can be attributed to the increased stiffness of the UGM in that direction, which is likely due to compaction effects, particle orientation, and deposition patterns. In general, under k_0 state condition, UGM stiffness tends to be higher in the vertical

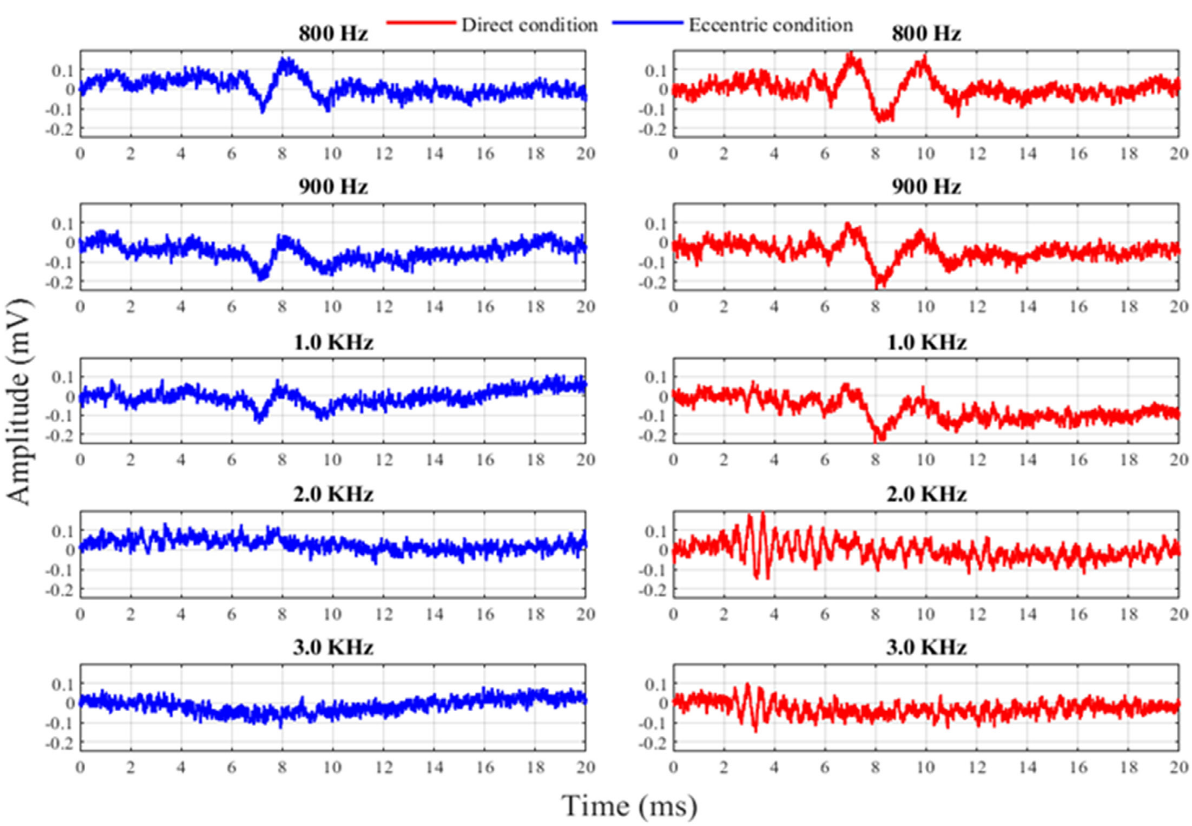

Figure 6. Output signals in eccentric transmission condition (blue color) and direct transmission condition (red color) for input frequencies ranging from 800Hz to 3 kHz.

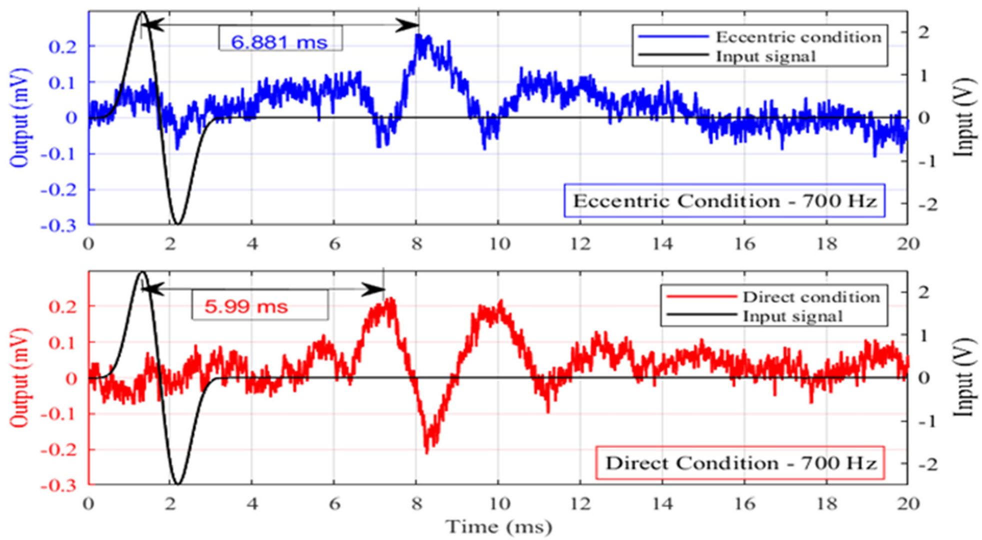

Figure 7. The traveling time of shear wave based on the peak-to-peak for direct and eccentric conditions.

direction compared to horizontal or inclined directions. This is primarily due to the fabric and particle orientation induced by compaction and gravitational forces.

2.2.2 Echo measurement configuration

The echo measurement configuration following the same approach of a previous study (Almukashfi et al., 2024) was tested using the 30 cm in diameter cylindrical cell for a 10 cm-thick UGM specimen ($D/H = 3$), as schematically presented in Figure 8. Based on Figure 8, the travel length between the transmitter and receiver bender elements can be calculated using Equation (3). Using the distances between the transmitter and receiver bender elements and between the reflecting boundary and the bender element tip, as shown in Figure 8, the shear wave travel length is calculated to be 169.17 mm according to Equation 3:

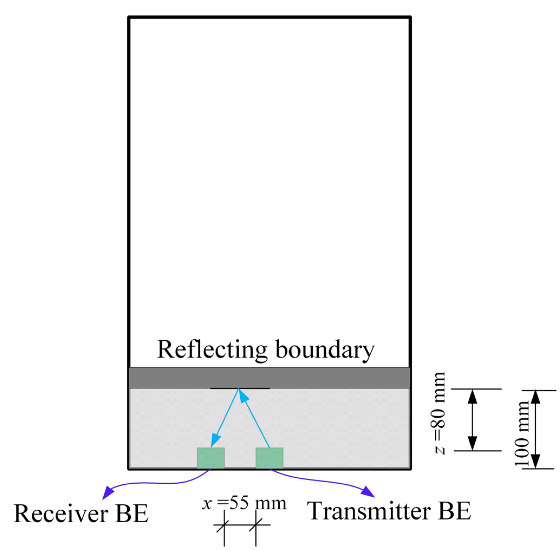

Figure 8. Echo measurement configuration for a 10 cm-thick UGM in the cylindrical cell.

$$l_e = \sqrt{x^2 + 4z^2} \tag{3}$$

where l_e is the shear wave travel length, x is the distance between the transmitter and receiver bender elements, and z is the distance between the reflecting boundary and the tip of the bender element.

Figure 9 presents typical output signals obtained from the echo measurement configuration. From the figure, it can be observed that the recorded signals exhibit two types of peaks. The first peak corresponds to the direct wave propagation, while the peaks beyond the first are associated with reflected shear waves. The recorded signals in this study, for a wave propagation travel length of 169.17 mm, are relatively consistent with the findings of a previous study conducted with a travel length of 118 mm in a Rowe cell device (Almukashfi et al., 2024). However, it should be noted that, in addition to the shorter wave propagation length and different material used in the previous study, the boundary conditions in the Rowe cell were more controllable compared to those in the current study. These differences may explain some of the discrepancies between the signals obtained in this study and those reported in the previous one (Almukashfi et al., 2024).

Overall, Figure 9 demonstrates that the echo measurement configuration is capable of capturing both direct and reflected wave propagation. Nevertheless, various factors, including boundary conditions, apparatus dimensions, and the distance between the transmitter and receiver bender elements, can

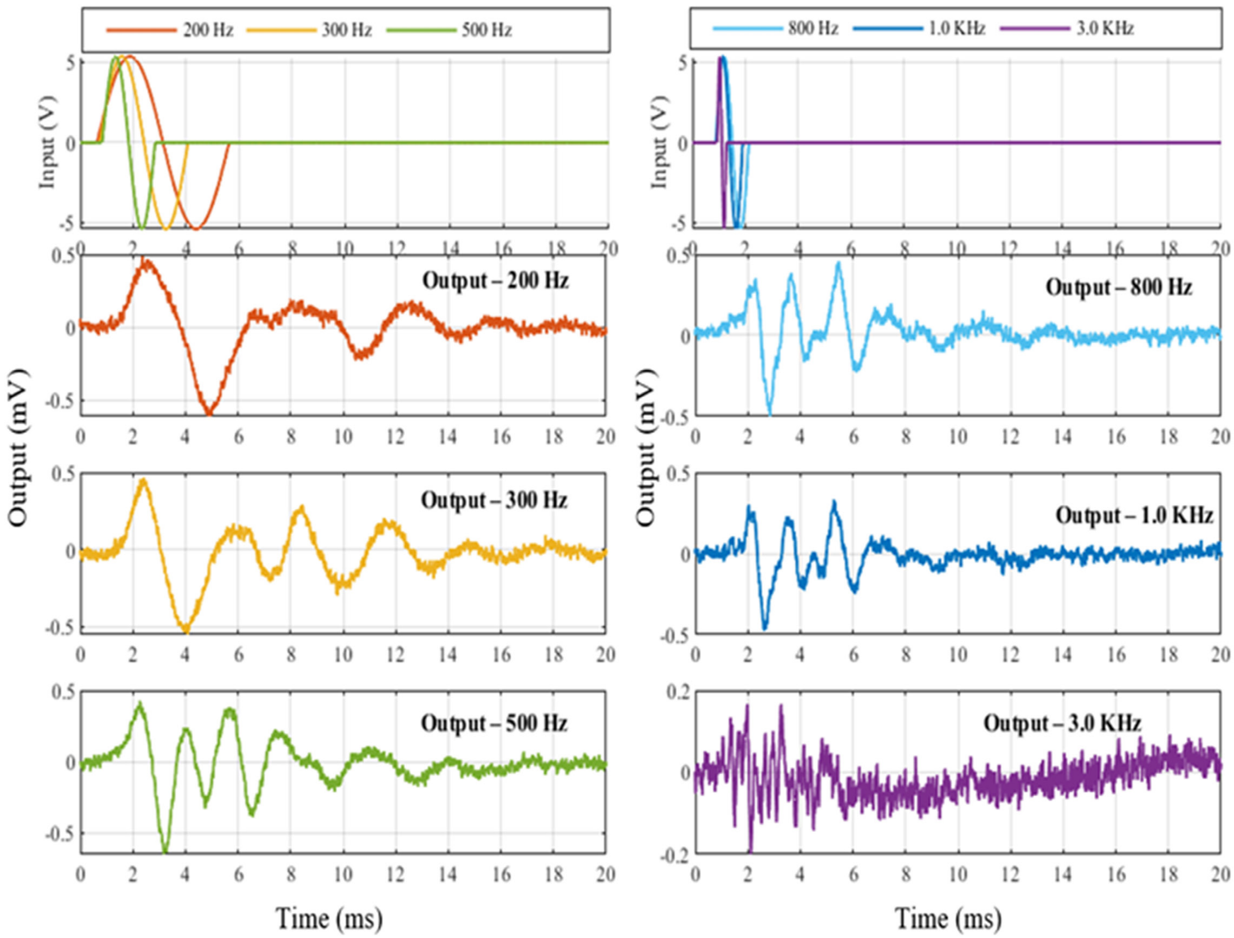

Figure 9. Input and output signals in echo measurement configuration.

influence the effectiveness of this configuration. Therefore, these factors should be further investigated in future studies.

2.2.3 Numerical modeling of bender element test using the GeoHyTE software

The bender element test is a simple and user-friendly geotechnical method for measuring the small-strain shear modulus of geomaterials based on shear wave propagation (Shirley & Hampton, 1978). However, accurate and precise interpretation of the shear wave arrival time from the recorded signals can be a challenging task (Yamashita et al., 2009).

One of the main reasons for this challenge is the interference between compressive (P) waves and shear (S) waves, as previously discussed in this study. To address this issue, several solutions have been proposed in the literature. These include experimental approaches such as the use of dissipative boundaries (Moldovan et al., 2025) and optimization of bender element configurations (Moldovan & Gomes Correia, 2021), as well as numerical investigations (Moldovan et al., 2021). Numerical modeling of the bender element test is effective for studying the influence of various parameters, as it allows full control over the testing conditions. To this end, different numerical techniques, including Discrete Element Modeling (DEM) (O'Donovan et al., 2015; Gu et al., 2020) and Finite Element Modeling (FEM) (Liu et al., 2022), have been employed to simulate shear wave propagation in geomaterials. However, numerical modeling using conventional techniques faces critical challenges such as mesh dependency and wavelength sensitivity (Roshan et al., 2024d). To overcome these issues, previous numerical studies have used very fine mesh sizes and small time steps. For example, the bender element test has been simulated using 2000 elements and a very small time step in the SOLVIA 90 package (Jovičić et al., 1996). In another study, a simulation using COMSOL software involved 5145 discretizing elements (Liu et al., 2022). However, the use of such fine meshes is not computationally efficient. Moreover, the correlation between experimental and numerical output signals has often been unsatisfactory (Johnson, 2011).

To address this limitation, the GeoHyTE software (Moldovan et al., 2024) was developed under the CEN-

DynaGEO (2022) and INTENT (Universidade Lusófona, 2023) projects. GeoHyTE is based on the hybrid Trefftz finite element method and is designed to simulate bender element tests with reliable accuracy using larger mesh sizes and reduced computational cost. This is affordable to hybrid-Trefftz finite elements due to their low wavelength sensitivity and compared to conventional finite elements. Moreover, the material model used in the software is a porous medium based on the Biot's theory, which is more consistent with the UGM used in this study. GeoHyTE determines the small-strain shear modulus of geomaterials by maximizing the correlation between experimental and numerical output signals. As a result, the shear modulus obtained using GeoHyTE is objective and numerically robust (Moldovan et al., 2024). In this study, GeoHyTE was employed to simulate the bender element test of the UGM described above. Figure 10 presents the mesh of the model, consisting of 655 hybrid-Trefftz elements. The numerical model's dimensions are based on the large-scale acrylic cylindrical cell ($B = 300$ mm and $H = 600$ mm) used for bender element testing of UGM. The mesh size varies depending on the location, with a finer mesh around the transmitter bender element and a maximum size of 40 mm. The geotechnical parameters of UGM discussed earlier were used in the numerical modeling.

Figure 11 illustrates the output signals under direct and eccentric conditions, based on both experiment and its numerical modelling, and using a 700 Hz input signal. The correlation between the signals is relatively good and the numerical model enables the straightforward identification of the arrival time of the shear wave, and consequently, the corresponding shear wave velocity and shear modulus of the UGM. Therefore, Figure 11 demonstrates that the GeoHyTE software can reliably model the bender element test for UGM.

The shear modulus of UGM obtained from numerical modelling is 18.5 MPa for the direct configuration and 13.5 MPa for the eccentric configuration. These values are close to those obtained from the experimental tests, 16.51 MPa and 12.76 MPa, respectively. The observed differences between numerical and experimental results can be attributed to the methods used for extracting shear wave arrival times. In the experimental test, the peak-to-peak method was used, whereas in numerical modelling, the cross-correlation method was applied. Moreover, in the experimental interpretation, the conversion of the propagation time into the shear modulus was made based on the theory of elasticity, while GeoHyTE uses the Biot's theory that takes into account the complex interplay between the various phases (solid and fluid) present in porous media. For the direct configuration, the difference in shear modulus between the numerical and experimental methods is 1.99 MPa, while for the eccentric configuration, the difference is smaller, 0.74 MPa. This smaller discrepancy in the eccentric condition can be attributed to reduced interference from compressive waves, which allows for a clearer shear wave signal. The findings are consistent with those of a previous study conducted on sand by Moldovan & Gomes Correia (2021).

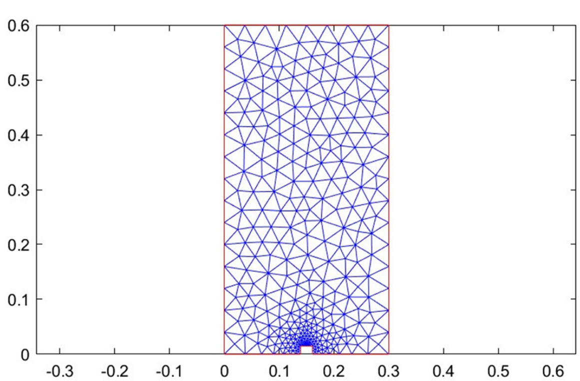

Figure 10. Finite element mesh employed in GeoHyTE software.

To illustrate the quality of the finite element solution obtained with GeoHyTE, Figure 12 presents the colour plot of the horizontal displacement field at the arrival time of the shear wave (S-wave). It is noted that the displacement amplitude of the input signal was of 10^{-6} m. As seen in Figure 12, the arrival of the shear wave is clearly identifiable. Additionally, Figure 12 also shows the scattered compressive wave, as indicated by the stress field. Therefore, the GeoHyTE software proves to be an efficient tool for simulating bender element tests and obtaining reliable shear modulus values in an objective rather than subjective manner.

To analyse the interference between the compressive wave and shear wave, the traces of these waves on the upper half of the testing cylinder are examined using the GeoHyTE software, as shown in Figure 13. The traces of the compressive and shear waves are defined as the maximum absolute values of the horizontal displacements u_x, calculated during the time interval t_a, measured from the onset of the wave propagation until the reflection of the shear wave from the top platen.

$$Tr(\boldsymbol{x}) = \max_{0 \le t \le t_a} u_x(\boldsymbol{x}, t) \tag{4}$$

An important feature of the hybrid-Trefftz finite elements is its capacity of filtering out wave types from the response of the structure (Moldovan & Gomes Correia, 2021). Exploiting this feature, Equations 5 and 6 define the compression and shear traces.

$$Tr_p(\boldsymbol{x}) = \max_{0 \le t \le t_a} u_{x_P}(\boldsymbol{x}, t) \tag{5}$$

$$Tr_s(\boldsymbol{x}) = \max_{0 \le t \le t_a} u_{x_S}(\boldsymbol{x}, t) \tag{6}$$

where $Tr_p(\boldsymbol{x})$ denotes the trace of the compressive wave, and $Tr_s(\boldsymbol{x})$ represents the trace of the shear wave, and u_{x_P} and u_{x_S} denote the horizontal displacements corresponding to the compressive and shear wave components, respectively.

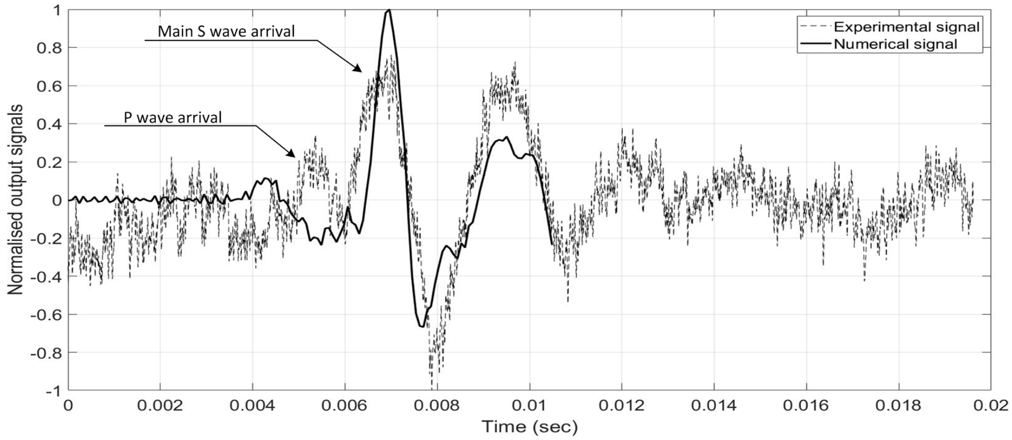

(a) Experimental and numerical output signals in direct configuration of bender element

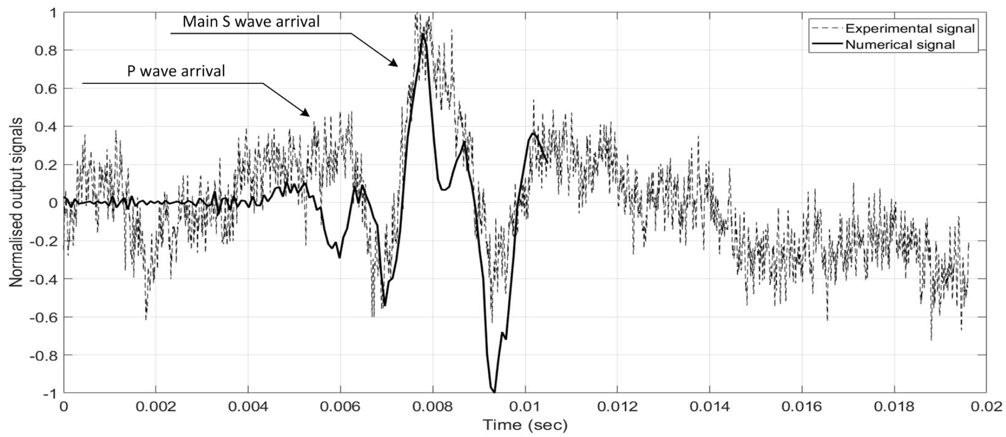

(b) Experimental and numerical output signals in eccentric configuration of bender element

Figure 11. Experimental and numerical output signals in different configuration of receiver bender element under 700 Hz: (a) direct configuration; (b) eccentric condition (one quarter of diameter).

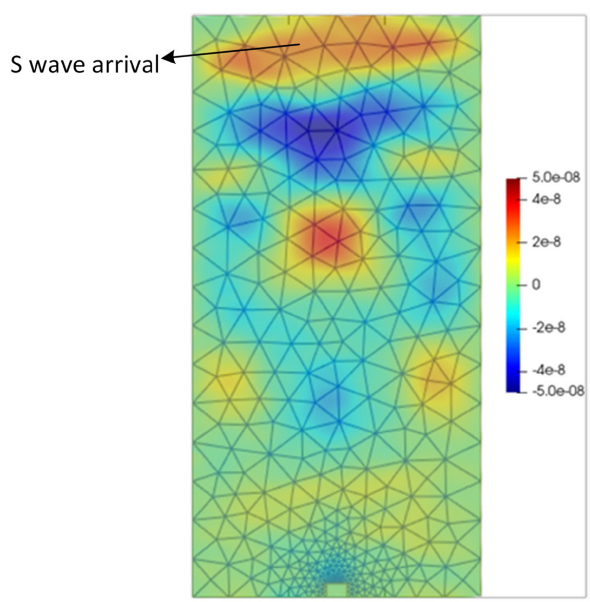

Figure 12. Stress fields at the arrival time of the S wave.

Figure 13a presents the combined traces of both compressive and shear waves in the upper half of the numerical model, while Figures 13b and 13c present the shear and compression traces. All figures are scaled between zero and 10^{-7} m of horizontal displacement. A comparison of Figures 13b and 13c indicates that the shear wave is more prominent than the compressive wave, which aligns with the actual behaviour observed in bender element tests. The shear wave intensity is much higher at the centre of the domain compared to the sides. This observation is consistent with previous findings that, although the eccentric configuration of the bender element reduces interference between compressive and shear waves, it also results in greater damping of the shear wave amplitude compared to the direct configuration, especially for low input frequencies.

3. Remote sensing for network -scale slope stability assessment

3.1 Methodology

The proposed framework for slope movement detection integrates ML algorithms with InSAR-derived satellite imagery to perform network-scale slope stability assessments. Vertical displacement time series extracted from InSAR were used to detect and forecast slope movements. The raw dataset comprises 5,079 records of vertical displacement measurements and acquisition dates spanning 2016-2023. A sample of the data is shown in Table 1. To prepare the data for modelling, the raw time series were first reformatted into a tabular structure, as shown in Table 2, and then a five-step sliding-window approach was applied. This procedure generated a training dataset with nine features: the four preceding displacement observations, their corresponding time intervals, and the target displacement to be predicted. Table 3 shows the final structure of the training dataset. Consequently, the last four displacement values and associated temporal differences serve as the input variables for forecasting the subsequent movement stage.

3.2 Models and assessment

A feed-forward artificial neural network (ANN) was developed in R (Owusu-Ansah et al., 2024; Venables et al., 2024) using the rminer package (Cortez, 2010; Owusu-Ansah et al., 2024) to predict vertical slope displacements.

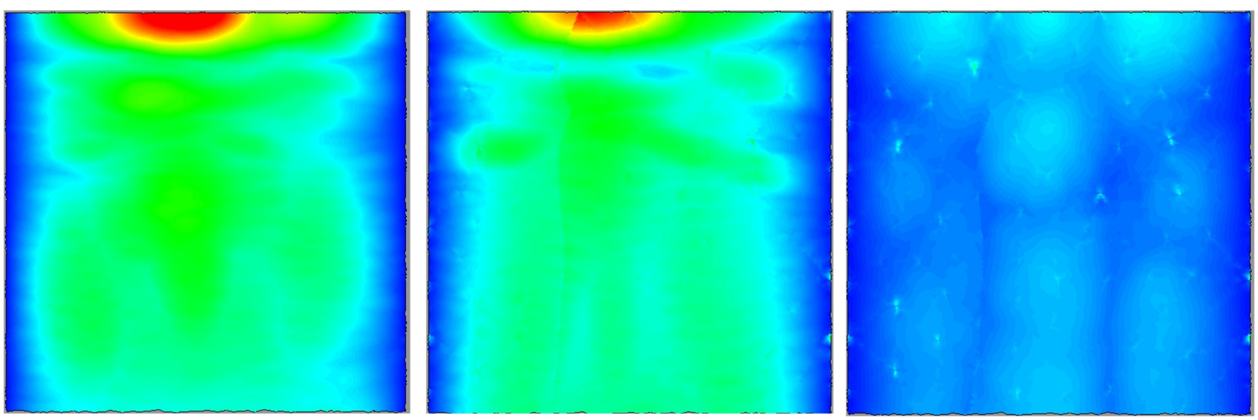

(a) S and P wave trace (b) S wave trace (c) P wave trace

Figure 13. The trace of S wave and P wave in the upper half of the model at the end of solution: (a) S and P wave trace; (b) S wave trace; (c) P wave trace.

Table 1. Raw records of InSAR vertical displacement.

FID	lon	latt	rmse	seas.	accel.	mean_vel.	max_ temporal_ coherence	20161016	20161028
1	-8.45	39.49	2.82	1.07	-0.34	-2.29	0.87	2.65	-1.91
2	-8.45	39.49	2.84	1.14	-0.35	-1.40	0.89	3.08	-1.32
3	-8.45	39.49	2.72	0.99	-0.09	-2.35	0.77	1.72	-1.77
4	-8.45	39.49	2.80	0.91	-0.72	-2.52	0.80	1.18	-2.78
…	…	…	…	…	…	…	…	…	…
5078	-8.38	40.18	2.58	1.29	0.45	-1.61	0.94	3.61	4.14
5079	-8.38	40.18	2.79	0.72	-1.33	1.00	0.88	1.66	4.67

Table 2. Sample dataset of InSAR vertical displacement (Owusu-Ansah et al., 2024).

Dates	PID1	PID2	PID3	PID4	PID5	PID6
16/10/2016	2.65	3.08	1.72	1.18	0.55	1.90
28/10/2016	-1.91	-1.32	-1.77	-2.78	-2.50	-1.13
09/11/2016	-1.73	-1.58	-2.88	-3.44	-2.94	-2.02
21/11/2016	-8.23	-8.25	-9.58	-9.71	-8.50	-6.38
03/12/2016	-5.01	-4.22	-5.29	-6.28	-6.90	-5.69
15/12/2016	1.88	2.11	0.63	-0.20	-0.77	0.26

Table 3. Sample of the new dataset (training dataset) produced by a sliding window of five (Owusu-Ansah et al., 2024).

Time1	Time2	Time3	Time4	Stage_1	Stage_2	Stage_3	Stage_4	Next stage (Output
12	12	12	12	2.65	-1.91	-1.73	-8.23	-5.01
12	12	12	12	-1.91	-1.73	-8.23	-5.01	1.88
12	12	12	12	3.08	-1.32	-1.58	-8.25	-4.22
12	12	12	12	-1.32	-1.58	-8.25	-4.22	2.11
24	24	24	24	-5.69	-8.90	-4.49	-9.77	-8.00
24	24	24	24	-8.90	-4.49	-9.77	-8.00	-4.81
24	24	24	24	-4.49	-9.77	-8.00	-4.81	-5.80
24	24	24	24	-9.77	-8.00	-4.81	-5.80	-1.73
72	72	72	72	-3.72	-5.55	-7.52	-8.21	-10.24
72	72	72	72	-5.55	-7.52	-8.21	-10.24	-4.60
72	72	72	72	-7.52	-8.21	-10.24	-4.60	-10.34
72	72	72	72	-8.21	-10.24	-4.60	-10.34	-14.12
144	144	144	144	-14.70	-15.02	-13.67	-16.49	-18.34
144	144	144	144	-10.11	-10.17	-9.34	-12.29	-13.67
144	144	144	144	-17.02	-16.28	-15.17	-17.02	-19.82
144	144	144	144	-15.67	-16.21	-15.12	-17.07	-20.22

The network was trained and validated via five-fold cross-validation procedure, and the entire process was repeated across five independent runs to ensure generalization. An ANN with a single hidden layer was employed, and the number of hidden neurons was optimized by a grid search over 1-10 neurons, with the best configuration chosen via five-fold cross-validation. By default, if no tuning is performed, the hidden layer contains five neurons.

Model performance was evaluated using four metrics: Mean Absolute Error (MAE), Mean Squared Error (MSE), Root Mean Squared Error (RMSE), and determinant coefficient (R^2). Lower MAE, MSE, and RMSE values indicate reduced predictive error, while higher R^2 values denote stronger agreement between observed and predicted displacements.

To interpret the ANN and identify the most influential predictors, a sensitivity analysis using relative importance was conducted (Cortez & Embrechts, 2011). This method assesses how changing each input variable affects the model's output, producing a score that ranks the input variables - the last four displacement measurements and their time intervals by their impact on prediction accuracy. By highlighting the highest-ranked inputs, this process reveals the key variables of slope movement and guides targeted feature selection and model refinement.

3.3 Results and discussion

Figure 14 shows the performance of the ANN model based on the previously described evaluation metrics. The results indicate strong predictive capability for vertical InSAR displacement time series, with an average MAE of 2.21, MSE of 8.20, RMSE of 2.86, and an R^2 value of 0.92. These values suggest that the model exhibits low error and variance, effectively capturing 92% of the variability in the observed displacements.

Figure 15 depicts the correlation plot between observed and predicted displacements. The points cluster tightly around the 1:1 line, and the fitted regression yields a determinant coefficient (R^2) of 0.92, confirming that over 90% of the variability in the observed data is captured by the ANN. This tight correlation underscores the model's ability to reproduce both the magnitude and temporal pattern of slope movements with acceptable accuracy.

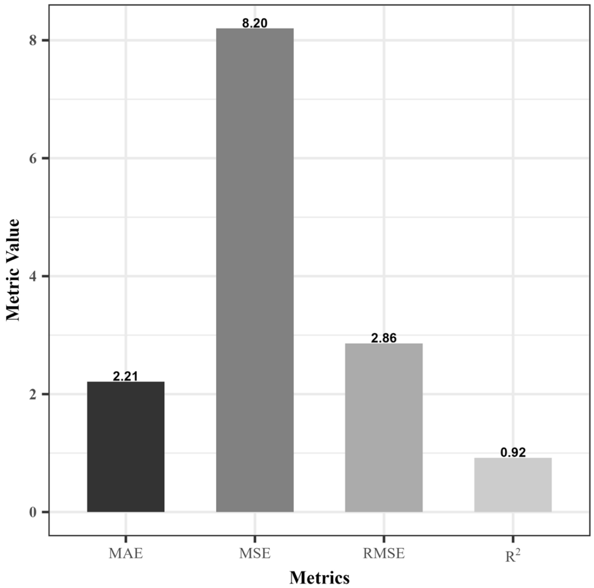

Figure 14. Model performance metrics (MAE, MSE, RMSE, R^2) for ANN on vertical InSAR data.

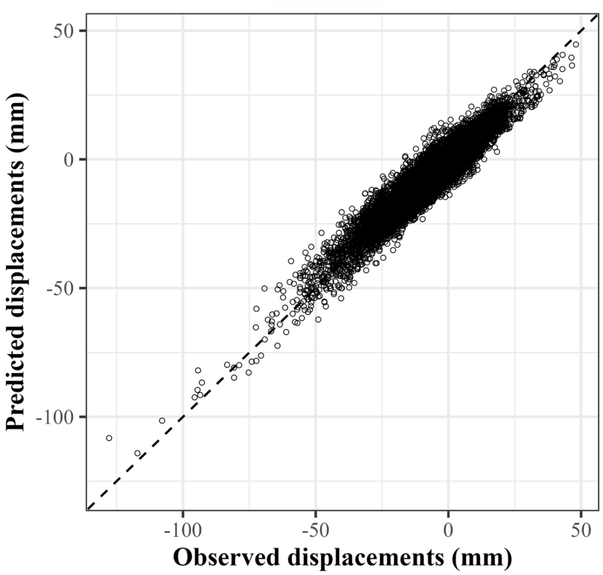

Figure 15. Scatterplot of observed vs. predicted displacements according to the ANN model.

To analyse ANN performance more closely, Figure 16 illustrates the model's capability to predict slope movements at time intervals of 12, 24, 48, and 72 days for three randomly selected slope points. The short-term forecasts (12 days) show excellent alignment with actual data, accurately reflecting both the trend and magnitude of movements. The 24-day predictions are better, with only slight increases in error. However, accuracy declines beyond this point: 48-day forecasts still perform better than the 72-day predictions. In contrast, the 72-day forecasts reveal significantly higher discrepancies from actual values. This decline in accuracy for longer time intervals highlights the cumulative propagation of uncertainty in time-series extrapolation and the ANN's dependence on recent displacement histories alone. These findings underscore the ANN model's effectiveness for short-term early-warning applications, while also highlighting the need for improvements in long-term slope stability forecasting. Although the model shows inferior accuracy for predictions at 48 and 72 days, it still successfully captures the overall trend in slope displacement, demonstrating its potential for monitoring evolving instability patterns over time.

A sensitivity analysis based on relative importance was performed to assess the contribution of each input variable to the prediction (Figure 17). The results identified the most recent displacement value (stage_4) as the dominant predictor, accounting for 34.86% of the model's output variance, followed by stage_3 at 19.70%. Inputs such as stage_1, Time4, and Time1 each contributed approximately 8-10%, while stage_2 (6.44%) and Time2 (5.77%) were the least influential.

These findings underscore the critical role of data recency in predictive performance. Recent displacement measurements have a significantly greater impact on forecast accuracy than the associated time intervals. From a practical standpoint, this highlights the value of increasing InSAR acquisition frequency to ensure timely updates, which can substantially enhance model reliability. Overall, the results support the potential of ANN models for real-time slope stability monitoring and early-warning systems.

4. Network-scale train-based bridge scour detection

4.1 Methodological framework

This research presents an innovative methodology for detecting and localizing scour around existing railway bridges using drive-by measurements. Expanding upon prior investigations (Tola et al., 2023b), the current study introduces a novel validation strategy by integrating field-acquired data with synthetically generated track profiles. Furthermore, it deviates from previous work by employing drive-by displacement measurements, in contrast to vehicle accelerations, and by utilizing data from an alternative sensor unit, rather than conventional measurement cars. Data acquisition unit, i.e., RILA (Rail Infrastructure Alignment Acquisition System), is a practical tool that enables fast coupling of any train in minutes. The case study field measurements for the scoured state could not be obtained for practical reasons (Tola et al., 2023b). Therefore, drive-by displacement data representing the damaged stage has been generated synthetically. A Cross-

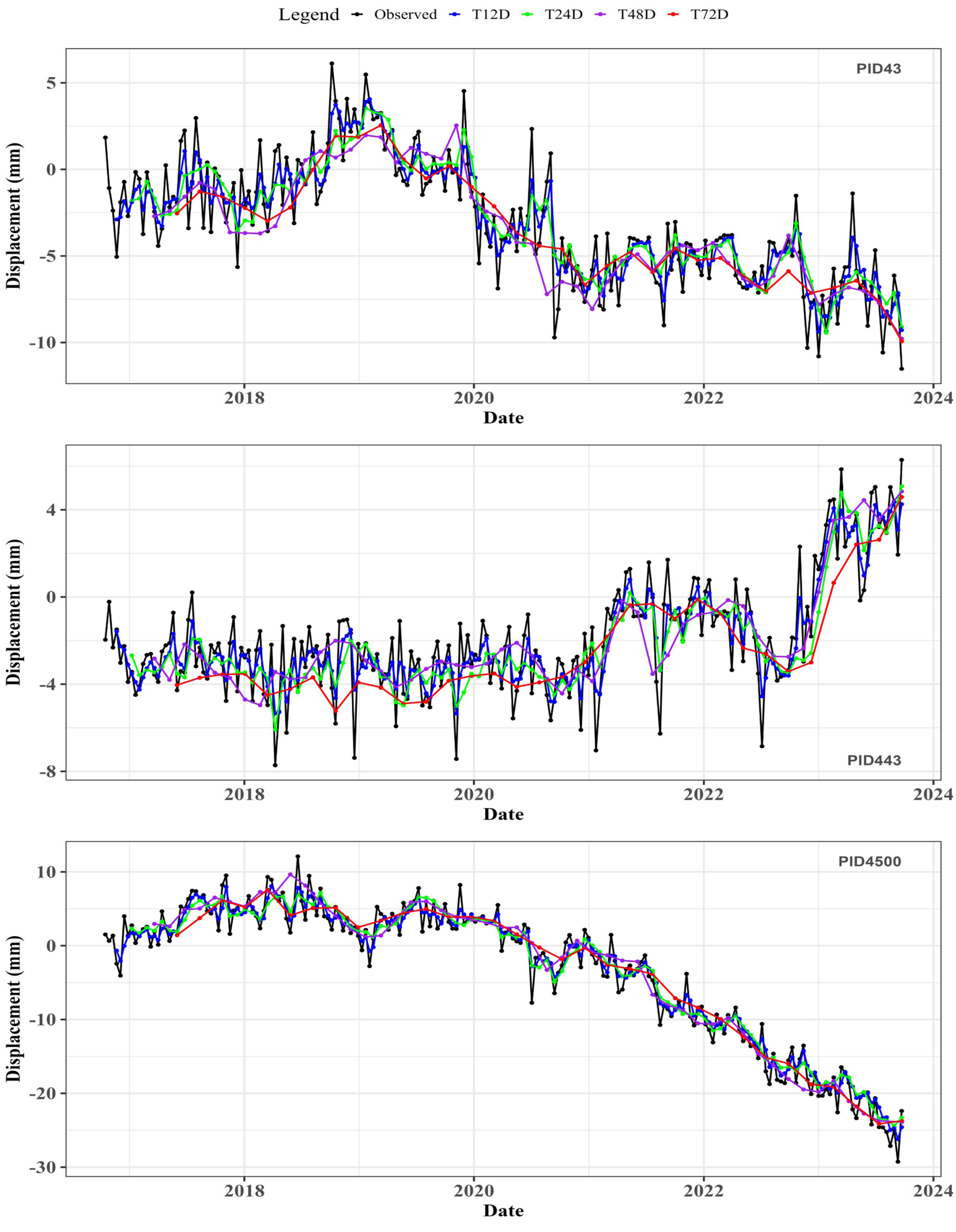

Figure 16. Time-series comparison of predicted displacements at 12-day, 24-day, 48-day, and 72-day intervals.

Entropy (CE) algorithm has been conducted to optimize pier stiffness by minimizing the sum of squared errors between theoretical and measured track profiles. The theoretical track profile is the superposition of the bridge displacement response under the moving load and rail irregularities extracted from the field measurements. The numerical model for obtaining the bridge displacement response adopts Moving Reference Influence Lines (MR-ILs). The disparity between inferred pier stiffness values for the scoured and healthy structural states serves as a primary indicator of scour. The procedural

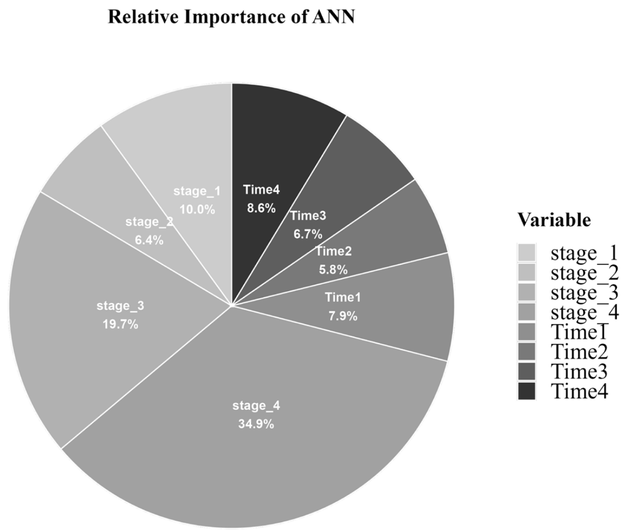

Figure 17. Relative importance of input variables, from stage_4 (34.86%) down to Time2 (5.77%).

framework of the developed methodology is illustrated in Figure 18a. Subsequently, the methodology has been extended for broader applicability to any railway bridge with longitudinal-level track measurements by applying ML models. Figure 18b shows the ongoing ML implementations. So far, Artificial Neural Network (ANN) models have been trained and tested using synthetically generated track profiles to enable the detection and localization of bridge scour. Details and future ML studies are explained in Section 4.3.

4.1.1 Numerical model adopting MR-IL

The numerical models explained in this section have been generated to calculate the bridge displacement component of the theoretical track profiles in the optimization phase. Track profile is the combination of the inherent rail irregularities and the bridge displacement response under the moving vehicle. The Finite Element model mimics the data acquisition system Rail Infrastructure Alignment Acquisition System (RILA),

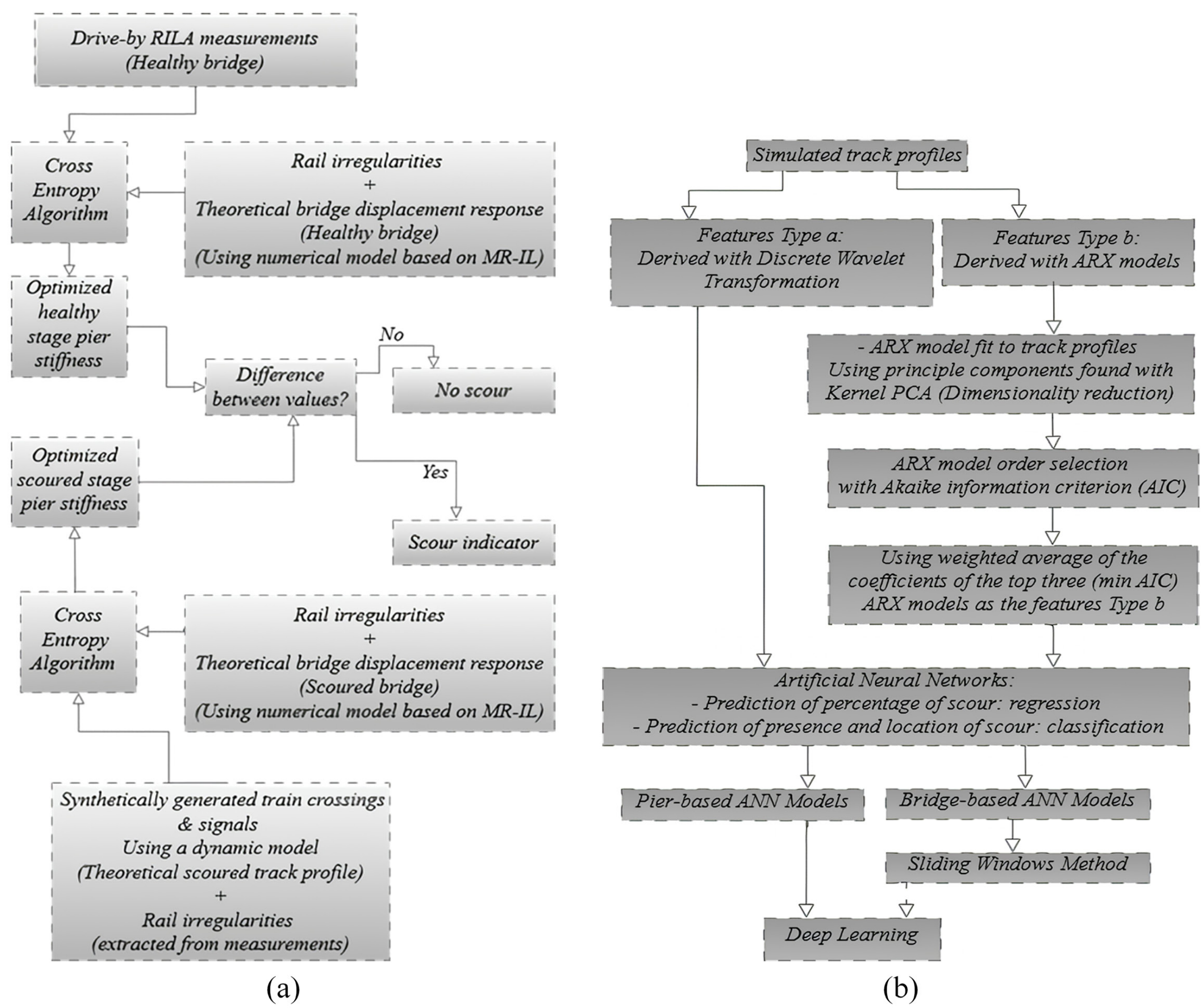

Figure 18. Flowcharts of the study: (a) Developed methodology, adapted from Tola et al. (forthcoming); (b) Extension to network level.

developed by Fugro, by the means of sensor location being at the front or at the back of the train. The model calculates displacement response using MR-ILs and the Virtual Work Theorem. The bridge piers are modelled as Winkler springs. Foundation scour is simulated by reducing the stiffness of the healthy stage pier. The stiffness of the piers (k_0) in the healthy condition is calculated by the formula of FEM) given in Equation 7:

$$k_0 = \beta_z \cdot \left[G_B / \left(1 - v\right) \right] \cdot \left[1.55 \cdot \left(L / B \right)^{0.75} + 0.8 \right] \tag{7}$$

where G_B is the soil shear modulus, v is the Poisson's ratio of the soil, L is the foundation length (m), B is its width (m), and β_z is the correction factor for embedment. Two finite element models have been developed to accommodate different sensor unit placements during train crossings, as the sensing equipment has been installed both at the front and rear of the train in different runs. More details are provided in (Tola et al., 2023a).

4.1.2 Cross-entropy optimization

The optimization of the pier stiffnesses corresponding to the healthy and scoured states of the bridge is achieved by employing a CE algorithm (Botev et al., 2013). The algorithm minimizes an objective function defined as the sum of the squared differences between measured and theoretical track profiles. The objective function ($O(k)$) is provided in Equation 8:

$$O(k) = \sum_{j=1}^{J} \sum_{n=1}^{N} \left(\delta_{ij}^{Measured} - \delta_{ij}^{Simulated} \right)^2 \tag{8}$$

where n represents the discretized beam elements along the bridge and j denotes the index over the number of train crossings (synthetically generated for scoured stages or field measured for healthy stages). In the case of scoured stage simulations, the term $\delta^{Measured}$ is replaced by $\delta^{Generated}$ to reflect the synthetic track profile. To account for variations due to sensor positioning, separate optimizations are performed for configurations where the RILA unit is placed at the front or rear of the train.

4.2 Application to a representative case study

The case study focuses on a multi-span simply supported railway bridge in the UK with a concrete superstructure supported by masonry piers and carrying two tracks. In-service measurements were taken using the RILA unit, which was mounted on a 6-axle train running along each track during regular operation. Ideally, longitudinal track profile measurements would be available before and after damage to compare pier stiffness over time directly. However, the available field data were collected after the bridge had undergone scour repair, so the measurements correspond only to the healthy state. Synthetic scour stage profiles were generated to demonstrate the effectiveness of the proposed scour detection method. For this purpose, the TTB-2D v4.4. model (Cantero, 2022), a VBI simulation tool that accounts for dynamic effects has been used to calculate bridge displacements under scoured conditions. These displacements have then been superimposed on rail irregularities extracted from field measurements to generate representative scoured track profiles. The theoretical track profiles have been similarly derived by combining the numerical bridge displacement responses (Section 4.1.2) with measured rail irregularities. Then, the CE algorithm has been performed to optimize pier stiffnesses of the damaged and undamaged bridge to check the indication of scour.

4.3 Extension to network-level scalability

The developed scour detection methodology is extended to a network level through the application of ML techniques, rendering it applicable to any railway bridge with available drive-by longitudinal track profile measurements. As illustrated in Figure 18b, the simulation dataset comprises approximately 1,000 runs across four bridges. These simulations vary train speed, axle weight, and scour severity (0-20%), bridge span length and number, considering single- and multiple-pier scour scenarios using the TTB-2D v.4.4 (Cantero, 2022), with rail profiles of FRA Class 5 and 6.

4.3.1 Future extraction

Two approaches were used to define the feature set. First, a fourth-level Daubechies Discrete Wavelet Transformation (db4 DWT) has been applied, and three parameters have been detected to be scour-sensitive (feature Type a). However, sensitivity analysis highlighted the dominance of a single parameter, motivating a complementary strategy based on ARX modelling. Kernel principal component analysis (PCA) has been applied to reduce dimensionality while retaining 95% of the variance. Then, ARX models have been fitted to the principal components using equal model orders, and the three components with the lowest AIC have been selected. Polynomial coefficients from the ARX have been aggregated by weighted averaging to form a refined set of input features. Unequal order ARX models were also explored for potential performance improvements. Derived polynomial coefficients have been used as Type b features of the ANN models.

4.3.2 ANN models

Two ANN architectures were developed: bridge-based and pier-based models. The bridge-based model aggregates input features over the entire bridge span, while the pier-based model localizes features around each pier, considering adjacent span sections. Each ANN was trained using one or two hidden layers with a single output neuron, using a 5% scour threshold for scour presence classification. The pier-based model architecture inherently allows scour localization by linking predictions to specific bridge piers.

The ongoing studies include incorporating rainfall data to establish a realistic scour calendar and applying the Sliding Windows method to analyze chronologically ordered data, with the prediction through the analysis of the temporal evolution of features extracted from sequential data segments, i.e., sliding windows.

4.4 Core results

Applying the proposed methodology to the case study described above revealed a significant difference in optimized pier stiffness between the healthy and damaged conditions, which indicated scour (Tola et al., 2023b). A sensitivity analysis has demonstrated that as the vertical support stiffness is reduced to represent increasing scour severity, the differences between the track profiles of the healthy and scoured stages become more pronounced. However, when measurement noise reaches 1% or higher, the damage indexes associated with unscoured piers tend to converge with those of the scoured pier. In the ML component of the study, the pier-based ANN models developed have demonstrated superior predictive performance compared to bridge-based models, with the most successful ones achieving accuracies of up to 70%. The ANN models are still under active development to enhance their accuracy and generalization capabilities. Although incorporating ARX-derived characteristics (Type b) has not substantially augmented conventional performance metrics, it facilitated a more equitable distribution of feature importance across DWT- and ARX-based inputs. This redistribution has been shown to reduce reliance on dominant features, thereby enhancing robustness and generalization across different bridge conditions while reducing the risk of overfitting. A more balanced feature utilisation has also been demonstrated to improve interpretability and stability, both critical for reliable network-scale scour detection.

5. Enhancing sustainability in transport infrastructure through BIM Integration

The reuse of construction and demolition waste (CDW) presents a promising opportunity for more sustainable practices in civil engineering, particularly in geotechnics. In recent work, efforts have been made to upcycle such materials, ranging from concrete to other forms of inert debris, by reintroducing them into transport infrastructure like roads and railways (Gomes Correia et al., 2025). Not only do these applications demonstrate the technical feasibility of using recycled aggregates in geotechnical layers, but they also highlight the environmental benefits of diverting significant amounts of CDW from landfills.

This increasing interest in CDW reuse intersects naturally with advancements in digital technologies, particularly with the growing adoption of BIM. The latter introduces the concept of a "digital twin" of built assets, encapsulating all relevant data about materials, structures, and construction sequences. When applied to the end-of-life phase of buildings, BIM becomes a powerful tool for identifying and cataloguing materials with reuse potential. Rather than relying on manual audits or generic estimates, BIM models provide detailed, object-level information that enables accurate material quantity take-offs, traceability, and strategic decision-making in waste reuse, as schematically presented in Figure 19 (Kuzminykh et al., 2023, 2024).

The RecycleBIM project builds upon the opportunity presented by the plenitude of information provided by BIM by proposing a fully integrated digital framework designed to manage CDW from a circular economy perspective. Its central goal is to transform demolition sites into resource hubs through enhanced data capture, model generation, and information sharing. At the core of the RecycleBIM approach is the use of cost-effective technologies—like handheld

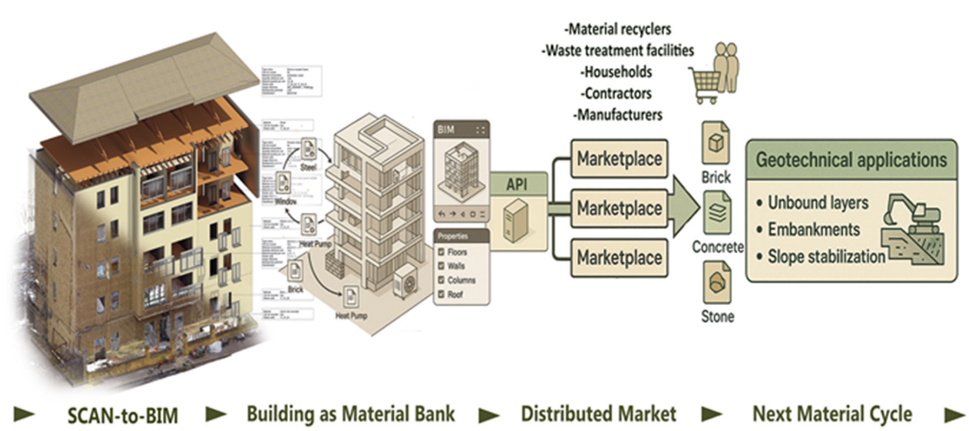

Figure 19. The RecycleBIM workflow and its applications to geotechnics.

LiDAR and lightweight surveys—to semi-automate the creation of BIM models for buildings slated for demolition. These models form the basis of downstream applications, supporting lifecycle assessments (LCA), lifecycle costing (LCC), demolition planning, and ultimately, material reuse.

One of RecycleBIM's most forward-looking components is its development of a distributed marketplace for CDW. By linking the information embedded in the digital models with a web-based platform, the project creates a digital environment where recovered resources can be cataloged, evaluated, and made available to potential buyers. The marketplace accommodates CDW in multiple forms: it can feature entire construction elements, or simply the constituent materials and inert aggregates that compose these elements. Each listing includes not only material-specific information but also environmental and cost-related metadata, along with geospatial referencing to facilitate local reuse and minimize transportation emissions.

Importantly, the marketplace is designed to integrate with demolition sequencing algorithms. The interest expressed by potential marketplace users in specific elements or materials may impose particular requirements on the demolition process—such as necessitating manual disassembly by human teams instead of mechanical demolition methods. This dynamic interaction ensures that the demolition planning process remains responsive to the reuse potential of the materials, thereby maximizing recovery rates while preserving material integrity. In general, Figure 19 presents the RecycleBIM workflow.

In the era of advanced technologies, traditional geotechnical investigation practices can be transformed into digital workflows through the implementation of BIM (Zhang et al., 2018). Throughout the lifecycle of a geotechnical project, BIM facilitates improved decision-making and enhanced collaboration across disciplines by integrating geotechnical data, including laboratory results, borehole logs, soil profiles, and health monitoring data, into a centralized digital model. The resulting BIM model enables predictive analysis for risk assessment, ground behavior, and the selection of construction methodologies (Fabozzi et al., 2021). Furthermore, BIM supports circular economy initiatives by reducing waste, enabling the reuse of materials in geotechnical projects, and optimizing the balance between excavation (cut-and-fill) and backfilling processes. For example, the RecycleBIM project (University of Minho, 2022) investigates strategies to reduce carbon footprints, increase resource efficiency, and enhance infrastructure resilience through the use of CDW materials in geotechnical applications. In this way, the RecycleBIM project (University of Minho, 2022) is aligned with several goals of the United Nations Sustainable Development Goals (SDGs).

This integrated marketplace holds significant promise for the geotechnical engineering sector. Given the growing use of recycled aggregates in geotechnical applications (fill material, reinforced soil structures (retaining walls and slopes), ground improvement) and transportation infrastructures (embankments, pavement and railway layers, noise barriers and landscape structures), RecycleBIM provides a critical mechanism for connecting supply (i.e., available waste materials) with demand (i.e., geotechnical project needs). Engineers and project managers can access detailed profiles on available materials—including information on type, volume, composition, and previous usage history, allowing for informed decisions regarding material suitability. Additionally, the platform supports standardization and quality assurance, addressing critical needs in sectors where material performance and reliability are paramount.

6. Conclusions and future directions

This study presents several advancements in digital technologies relevant to transportation geotechnics. These technologies range from advanced geomaterials to innovative testing, computational methods, AI-, Data-, and BIM approaches. In summary, the following conclusions can be drawn from the findings of this study:

- Novel geomaterials used in transportation geotechnics must not only withstand the applied loading from traffic but also provide additional functionality. In this regard, electrically conductive cementitious composites offer innovative alternatives to conventional cementitious materials. The self-sensing cementitious geomaterials developed at the University of Minho not only stabilize transportation layers but also enable additional functionalities such as traffic monitoring, damage detection, and self-heating for snow and ice melting. However, it is crucial to consider several factors in their mix design and application, including the content and type of conductive fillers, dispersion quality, electrode configuration, and measurement systems, among others;
- The bender element test is a simple and user-friendly geotechnical method widely used in transportation geotechnics. However, previous studies have primarily employed small-scale testing setups. To address this limitation, a novel large-scale chamber equipped with various bender element configurations was developed at the University of Minho to conduct bender element tests on unbound granular materials (UGMs), which are coarse-grained and more representative of actual field conditions in unbound granular layers;
- Based on the bender element tests, it was observed that the irregularity and interference between compressive and shear waves in the output signals were lower under the eccentric configuration compared to the direct configuration. However, the signal attenuation was higher in the eccentric configuration due to the longer wave travel path, which increases energy loss from scattering and damping;

- The echo measurement configuration demonstrated that reflected shear waves can be effectively captured by the receiver bender element. However,future studies should investigate additional influencing factors, such as the ratio of specimen thickness to diameter, boundary conditions, and material type, to better understand the applicability of this method;
- The developed computational software, GeoHyTE, is an efficient numerical tool for simulating bender element experiments. Built upon the Hybrid Trefftz finite element method, the software calculates the travel time of shear waves and the corresponding small-strain shear modulus based on shear wave velocity. It does this by maximizing the correlation between experimental and numerical output signals. As a result, the shear modulus determined using GeoHyTE is objective and reliable;
- The integrating the learning capabilities of Artificial Neural Networks (ANNs) with the wide spatial coverage of satellite imagery, particularly InSAR data, can effectively support slope monitoring and prediction at the scale of transportation networks. The developed ANN model successfully forecasted vertical displacements, achieving a mean absolute error of 2.21, mean squared error of 8.20, root mean squared error of 2.86, and an R^2 of 0.92. A sensitivity analysis based on relative importance highlighted the dominant role of the most recent displacement input (stage_4), which accounted for 34.86% of the model's predictive influence, followed by stage_3 at 19.70%. These results suggest that increasing the frequency of InSAR acquisitions to ensure timely displacement updates can significantly enhance prediction accuracy. Overall, the strong predictive performance and interpretable results confirm the potential of ANN-based models for real-time slope stability monitoring and early-warning applications;
- Demonstration of the feasibility of an indirect, train-based framework for network-scale scour detection in railway bridges. The research under discussion effectively combines physical modelling, optimization, and machine learning approaches, enabling scalable and cost-effective scour detection. Subsequent research will concentrate on integrating deep learning ML models, such as Convolutional Neural Networks (CNNs). Additionally, the implementation of blind testing on unseen bridges and the development of traffic light warning systems will be undertaken. The subsequent steps are intended to enhance the robustness of predictions and facilitate real-time decision-making capabilities for railway infrastructure managers;
- The integration between BIM-enabled demolition workflows and material reuse in geotechnics offers a novel pathway for achieving sustainability goals in transportation geotechnics. RecycleBIM bridges the gap between digital construction tools and sustainable geotechnical practices by embedding circularity at the core of the demolition process, it paves the way for a smarter, greener, and more resource-efficient construction ecosystem.

Acknowledgements

The author(s) acknowledge(s) the financial support of the Foundation for Science and Technology (FCT) through the project UIDB/04625/2025 of the research unit CERIS. The second and third authors also acknowledge the Foundation for Science and Technology (FCT) for financial support under the references 2023.03777.BD, and the INTENT project (2022.06879.PTDC), respectively. This work was partly financed by FCT/MCTES through national funds (PIDDAC) under the R&D Unit Institute for Sustainability and Innovation in Structural Engineering (ISISE), under reference UID/04029/ Institute for Sustainability and Innovation in Structural Engineering (ISISE), and under the Associate Laboratory Advanced Production and Intelligent Systems ARISE under reference LA/P/0112/2020. Also, this work is financed by national funds through FCT – Foundation for Science and Technology, under grant agreement CEECINST/00018/2021 and 2021.06162.BD attributed to the fourth and sixth authors, respectively. This work was also partially funded by the ERA-MIN 3 project RecycleBIM (ERA-MIN3/0006/2021), whose funding comes from the European Union under the Horizon 2020 Programme through Grant Agreement No. 101003575 of the European Commission and Fundação para a Ciência e Tecnologia - FCT (https://doi.org/10.54499/ERA-MIN3/0006/2021). The research was also partially financed within the European Horizon 2020 Joint Technology Initiative Shift2Rail, under contract number 101012456 (IN2TRACK3). In addition, this work was also carried out under the "HILLS-AI" Project, by the "TecMinho-Spotlite" consortium. Special acknowledgment is extended to Ricardo Cabral, on behalf of Spotlite, for providing the InSAR data used in this study, as well as to Professors Eugene O'Brien and José Matos for their guidance and support. Moreover, José Granja and Artur Kuzminykh are also acknowledged by their contributions to the BIM-related topics at issue in this work. The authors gratefully acknowledge the support of Network Rail for supplying structural bridge information and enabling the acquisition of in-service monitoring data from Fugro, both of which were instrumental in advancing this research.

Declaration of interest

The authors have no conflicts of interest to declare. All co-authors have observed and affirmed the contents of the paper and there is no financial interest to report.

Authors' contributions

António Gomes Correia: conceptualization, methodology, investigation, formal analysis, validation, supervision, resources, funding acquisition, writing – original draft, writing – review & editing. Mohammad Jawed Roshan: conceptualization, data curation, methodology, investigation, formal analysis, visualization, software, writing – original draft, experimental testing. Ionut Dragos Moldovan: conceptualization, methodology, investigation, formal analysis, validation, supervision, resources, funding acquisition, writing – original draft, writing – review & editing. Joaquim Tinoco: conceptualization, methodology, investigation, formal analysis, validation, supervision, resources, funding acquisition, writing – review & editing. Dominic Owusu-Ansah: conceptualization, data curation, methodology, investigation, formal analysis, visualization, software, writing – original draft. Sinem Tola: conceptualization, data curation, methodology, investigation, formal analysis, visualization, software, writing – original draft. Manuel Parente: conceptualization, data curation, methodology, investigation, formal analysis, visualization, software, writing – original draft. Miguel Azenha: conceptualization, methodology, investigation, formal analysis, validation, supervision, resources, funding acquisition, writing – review & editing.

Data availability

All data produced or examined in the course of the current study are included in this article.

Declaration of use of generative artificial intelligence

This work was not prepared with the assistance of Generative Artificial Intelligence (GenAI).

List of symbols and abbreviations

k_0	Stiffness of the piers
j	Index over the number of train crossings
l_e	Shear wave travel length
n	Discretized beam element
t_a	Time interval
u_{x_S}	Horizontal displacement corresponding to shear wave
u_{x_P}	Horizontal displacement corresponding to compressive wave
x	Distance between transmitter and receiver bender elements
z	Distance between the reflecting boundary and the tip of the bender element
AI	Artificial intelligence
ANN	Artificial neural network
AUC	Area under curve
AIC	Akaike Information Criterion
ARX	AutoRegressive with eXogenous input
B	Width
BIM	Building information modeling
BE	Bender element
CNNs	Convolutional neural networks
CDW	Construction and demolition waste
CB	Carbon black
CF	Carbon fiber
CNT	Carbon nanotube
CNF	Carbon nanofiber
CNM	Carbon nanomaterial
CE	Cross entropy
CERIS	Civil engineering research and innovation for sustainability
D	Diameter
DIC	Digital image correlation
DEM	Discrete element modeling
db4 DWT	Daubechies 4 Discrete Wavelet Transformation
DWT	Discrete Wavelet Transform
EU	European union
FCR	Fractional change in resistance
FEM	Finite element modeling
FCT	Foundation for Science and Technology
FID	Field ID
FRA	Federal Railroad Administration
G_B	Soil shear modulus
GP	Graphite powder
GNP	Graphene nanoplatelet
H	Height
InSAR	Interferometric Synthetic Aperture Radar
ISISE	Institute for sustainability and innovation in structural engineering
INTENT	Intelligent health monitoring of road infrastructures using bender elements embedded in pavements
ISISE	Institute for sustainability and innovation in structural engineering
L	Foundation length
LCA	lifecycle assessment
LCC	Lifecycle cost
LA/P	Laboratório Associado de Produção Avançada e Sistemas Inteligentes
Latt	Latitude
Lon	Longitude
ML	Machine learning
MAE	Mean absolute error
MCTES	Ministry of Science, Technology and Higher Education
MR-ILs	Moving reference influence lines
MSE	Mean squared error
mean_vel	Mean Velocity
M_r	Resilient modulus
MWCNT	Multi-walled carbon nanotube
$O(k)$	Objective function

P	Compressive wave
PCA	principal component analysis
PID	Point ID
PIDDAC	Programa de Investimentos e Despesas de Desenvolvimento da Administração Central
PIV	Particle image velocimetry
R^2	Determination coefficient
R_0	Initial resistance
R_i	Resistance at certain loading level
RCDWs	Recycled construction and demolition wastes
RILA	Rail infrastructure alignment acquisition system
RMSE	Root mean squared error
S	Shear wave
SAR	synthetic aperture radar
SDGs	Sustainable Development Goals
Seas	Seasonality
SHM	Structural health monitoring
$Tr(\boldsymbol{x})$	Trace of the wave
$Tr_p(\boldsymbol{x})$	Trace of compressive wave
$Tr_s(\boldsymbol{x})$	Trace of shear wave
TTB-2D	Train-Track-Bridge 2D simulation model
UGM	Unbound granular material
UK	United Kingdom
UIDB	Unidade de Investigação e Desenvolvimento Base
VBI	Vehicle Bridge Interaction
βz	Correction factor for embedment
$\delta^{Measured}$	Measured track profile
$\delta^{Generated}$	Generated track profile
ε_r	Resilient strain
σ_d	Deviator stress
v	Poisson's ratio
ΔR	Changes in resistance

References

Almukashfi, A.M.A., Castellanza, R., Gomes Correia, A., Arroyo, M., Zuretti, C., Bendea, D., & Moldovan, I.D. (2024). A modified rowe cell with bender elements for small strain shear modulus measurements. *Geotechnical Testing Journal*, 47(5), 985-1005. http://doi.org/10.1520/GTJ20230329.

Arulnathan, R., Boulanger, R., & Riemer, M. (1998). Analysis of bender element tests. *Geotechnical Testing Journal*, 21(2), 120-131. http://doi.org/10.1520/GTJ10750J.

Bao, T., Andrew Swartz, R., Vitton, S., Sun, Y., Zhang, C., & Liu, Z. (2017). Critical insights for advanced bridge scour detection using the natural frequency. *Journal of Sound and Vibration*, 386, 116-133. http://doi.org/10.1016/j.jsv.2016.06.039.

Barker, L., Hannaford, J., Muchan, K., Turner, S., & Parry, S. (2016). The winter 2015/2016 floods in the UK: a hydrological appraisal weather. *Weather*, 71(12), 324-333. http://doi.org/10.1002/wea.2822.

Borke Birgin, H., D'Alessandro, A., Favaro, M., Sangiorgi, C., Laflamme, S., & Ubertini, F. (2022). Field investigation of novel self-sensing asphalt pavement for weigh-in-motion sensing. *Smart Materials and Structures*, 31(8), 085004. http://doi.org/10.1088/1361-665X/ac7922.

Botev, Z.I., Kroese, D.P., Rubinstein, R.Y., & L'Ecuyer, P. (2013). The cross-entropy method for optimization. In C.R. Rao (Ed.), *Handbook of statistics. Machine learning: theory and applications* (pp. 35-59). Elsevier.

Cantero, D. (2022). TTB-2D: Train–Track–Bridge interaction simulation tool for Matlab. *SoftwareX*, 20, 101253. http://doi.org/10.1016/j.softx.2022.101253.

CEN-DynaGEO. (2022). *Coupled experimental and numerical approaches toward reliable dynamic characterization of multi-phase geomaterials*. Retrieved in May 4, 2025, from https://sites.google.com/view/cen-dynageo/home?authuser=0

Cortez, P. (2010). Data mining with neural networks and support vector machines using the R/rminer tool. In P. Perner (Ed.), *Advances in data mining. applications and theoretical aspects* (Lecture Notes in Computer Science, Vol. 6171, pp. 572-583). Berlin: Springer.

Cortez, P., & Embrechts, M.J. (2011). Opening black box data mining models using sensitivity analysis. In *Proceedings of the 2011 IEEE Symposium on Computational Intelligence and Data Mining (CIDM)* (pp. 341-348). IEEE. http://doi.org/10.1109/CIDM.2011.5949423.

Di Traglia, F., Nolesini, T., Ciampalini, A., Solari, L., Frodella, W., Bellotti, F., Fumagalli, A., De Rosa, G., & Casagli, N. (2018). Tracking morphological changes and slope instability using spaceborne and ground-based SAR data. *Geomorphology*, 300, 95-112. http://doi.org/10.1016/j.geomorph.2017.10.023.

Ding, S., Xiang, Y., Ni, Y.-Q., Thakur, V.K., Wang, X., Han, B., & Ou, J. (2022). In-situ synthesizing carbon nanotubes on cement to develop self-sensing cementitious composites for smart high-speed rail infrastructures. *Nano Today*, 43, 101438. http://doi.org/10.1016/j.nantod.2022.101438.

Elsaid, A., & Seracino, R. (2014). Rapid assessment of foundation scour using the dynamic features of bridge superstructure. *Construction & Building Materials*, 50, 42-49. http://doi.org/10.1016/j.conbuildmat.2013.08.079.

European Comission. (2020). *A new Circular Economy Action Plan* (European Commission Report, No. 98). Luxembourg.

European Comission. (2021). *IN2TRACK2: research into enhanced track and switch and crossing system 2*. Retrieved in May 4, 2025, from https://cordis.europa.eu/project/id/826255

European Comission. (2023). *IN2TRACK3: research into optimised and future railway infrastructure*. Retrieved in May 4, 2025, from https://cordis.europa.eu/project/id/101012456

Fabozzi, S., Biancardo, S.A., Veropalumbo, R., & Bilotta, E. (2021). I-BIM based approach for geotechnical and numerical modelling of a conventional tunnel excavation. *Tunnelling and Underground Space Technology*, 108, 103723. http://doi.org/10.1016/j.tust.2020.103723.

Fernandes, T., Lopez, R., & Ribeiro, D. (2024). Drive-by scour damage detection in railway bridges using deep autoencoder and different sensor placement strategies. *Journal of Civil Structural Health Monitoring*, 14(8), 1895-1916. http://doi.org/10.1007/s13349-024-00821-w.

Fitzgerald, P.C., Malekjafarian, A., Cantero, D., O'Brien, E.J., & Prendergast, L.J. (2019). Drive-by scour monitoring of railway bridges using a wavelet-based approach. *Engineering Structures*, 191, 1-11. http://doi.org/10.1016/j.engstruct.2019.04.046.

Frodella, W., Salvatici, T., Pazzi, V., Morelli, S., & Fanti, R. (2017). GB-InSAR monitoring of slope deformations in a mountainous area affected by debris flow events. *Natural Hazards and Earth System Sciences*, 17(10), 1779-1793. http://doi.org/10.5194/nhess-17-1779-2017.

Gomes Correia, A., & Gastine, E. (2024). How AI and IoT are transforming geotechnical site monitoring and construction. In N. Guerra, M. M. Fernandes, C. Ferreira, A. Gomes Correia, A. Pinto & P.S. Pinto (Eds.), *Geotechnical engineering challenges to meet current and emerging needs of society* (pp. 72-83). London: CRC Press. http://doi.org/10.1201/9781003431749-4.

Gomes Correia, A., & Roshan, M.J. (2024). Self-sensing cementitious geocomposites in rail track substructures. *Transportation Geotechnics*, 46, 101260. http://doi.org/10.1016/j.trgeo.2024.101260.

Gomes Correia, A.G., Winter, M.G., Fortunato, E.C., Roque, A.J., Parente, M., & Azenha, M. (2025). The beneficial management of granular waste materials for roads and railways. In B. Indraratna, Y. Qi & C. Rujikiatkamjorn (Eds.), *Waste materials utilisation for transport infrastructure* (pp. 134-148). London: CRC Press. http://doi.org/10.1201/9781003307211-9.

Gu, X., Liang, X., Shan, Y., Huang, X., & Tessari, A. (2020). Discrete element modeling of shear wave propagation using bender elements in confined granular materials of different grain sizes. *Computers and Geotechnics*, 125, 103672. http://doi.org/10.1016/j.compgeo.2020.103672.

Ha, D.W., Kim, J.M., Kim, Y., & Park, H.S. (2018). Development and application of a wireless MEMS-based borehole inclinometer for automated measurement of ground movement. *Automation in Construction*, 87, 49-59. http://doi.org/10.1016/j.autcon.2017.12.011.

Hajializadeh, D. (2022). Deep-learning-based drive-by damage detection system for railway bridges. *Infrastructures*, 7(6), 84. http://doi.org/10.3390/infrastructures7060084.

Han, B., Yu, X., & Kwon, E. (2009). A self-sensing carbon nanotube/cement composite for traffic monitoring. *Nanotechnology*, 20(44), 445501. http://doi.org/10.1088/0957-4484/20/44/445501.

Han, D., Kalantari, M., & Rajabifard, A. (2021). Building Information modeling (bim) for construction and demolition waste management in Australia: a research agenda. *Sustainability*, 13(23), 12983. http://doi.org/10.3390/su132312983.

Hoang, N.-D., Liao, K.-W., & Tran, X.-L. (2018). Estimation of scour depth at bridges with complex pier foundations using support vector regression integrated with feature selection. *Journal of Civil Structural Health Monitoring*, 8(3), 431-442. http://doi.org/10.1007/s13349-018-0287-2.

Hong, C.-Y., Zhang, Y.-F., Zhang, M.-X., Leung, L.M.G., & Liu, L.-Q. (2016). Application of FBG sensors for geotechnical health monitoring, a review of sensor design, implementation methods and packaging techniques. *Sensors and Actuators. A, Physical*, 244, 184-197. http://doi.org/10.1016/j.sna.2016.04.033.

Huang, A.-B., Lee, J.-T., Ho, Y.-T., Chiu, Y.-F., & Cheng, S.-Y. (2012). Stability monitoring of rainfall-induced deep landslides through pore pressure profile measurements. *Soil and Foundation*, 52(4), 737-747. http://doi.org/10.1016/j.sandf.2012.07.013.

Huang, Y., Li, H., & Qian, S. (2018). Self-sensing properties of engineered cementitious composites. *Construction & Building Materials*, 174, 253-262. http://doi.org/10.1016/j.conbuildmat.2018.04.129.

Jiao, W., Sha, A., Liu, Z., Jiang, W., Hu, L., & Qin, W. (2023). Analytic investigations of snow melting efficiency and temperature field of thermal conductive asphalt concrete combined with electrical-thermal system. *Journal of Cleaner Production*, 399, 136622. http://doi.org/10.1016/j.jclepro.2023.136622.

Johnson, S. (2011). *Modeling a bender element test using Abaqus finite element program* [Doctoral thesis]. Massachusetts Institute of Technology.

Jovičić, V., Coop, M.R., & Simić, M. (1996). Objective criteria for determining G max from bender element tests. *Geotechnique*, 46(2), 357-362. http://doi.org/10.1680/geot.1996.46.2.357.

Kang, K., Besklubova, S., Dai, Y., & Zhong, R.Y. (2022). Building demolition waste management through smart BIM: a case study in Hong Kong. *Waste Management*, 143, 69-83. http://doi.org/10.1016/j.wasman.2022.02.027.

Kang, M., Qamhia, I.I.A., Tutumluer, E., Hong, W.-T., & Tingle, J.S. (2021). Bender element field sensor for the measurement of pavement base and subbase stiffness characteristics. *Transportation Research Record: Journal of the Transportation Research Board*, 2675(8), 394-407. http://doi.org/10.1177/0361198121998350.

Kang, M., Wang, H., Qamhia, I.I.A., Tutumluer, E., Garg, N., Villafane, W., & Murrell, S. (2023). Evaluation of airport pavement base layer stiffness characteristics via embedded field sensors. *Transportation Research Record: Journal of the Transportation Research Board*, 2677(8), 462-473. http://doi.org/10.1177/03611981231156938.

Kang, Z., Zhang, J., Li, N., Yang, Y., Lv, T., & Lu, J. (2024). Development of self-sensing cement composites by incorporating hybrid biochar and nano carbon black.

Cement and Concrete Composites, 153, 105708. http://doi.org/10.1016/j.cemconcomp.2024.105708.

Khan, M.A., McCrum, D.P., Prendergast, L.J., O'Brien, E.J., Fitzgerald, P.C., & Kim, C.-W. (2021). Laboratory investigation of a bridge scour monitoring method using decentralized modal analysis. *Structural Health Monitoring*, 20(6), 3327-3341. http://doi.org/10.1177/1475921720985122.

Kuzminykh, A., Granja, J., Parente, M., & Azenha, M. (2024). Promoting circularity of construction materials through demolition digitalisation at the preparation stage: information requirements and openBIM-based technological implementation. *Advanced Engineering Informatics*, 62, 102755. http://doi.org/10.1016/j.aei.2024.102755.

Kuzminykh, A., Parente, M., Vieira, V., Granja, J., & Azenha, M. (2023). RecycleBIM approach towards integrated data management for circularity. In A. Jędrzejewska, F. Kanavaris, M. Azenha, F. Benboudjema & D. Schlicke (Eds.), *Proof of concept in a RC building* (pp. 252-262). Cham: Springer.

Lee, J.-S., & Santamarina, J.C. (2005). Bender elements: performance and signal interpretation. *Journal of Geotechnical and Geoenvironmental Engineering*, 131(9), 1063-1070. http://doi.org/10.1061/(ASCE)1090-0241(2005)131:9(1063).

Lin, T.-K., & Chang, Y.-S. (2017). Development of a real-time scour monitoring system for bridge safety evaluation. *Mechanical Systems and Signal Processing*, 82, 503-518. http://doi.org/10.1016/j.ymssp.2016.05.040.

Liu, H., Cascante, G., Maghoul, P., & Shalaby, A. (2022). Experimental investigation and numerical modeling of piezoelectric bender element motion and wave propagation analysis in soils. *Canadian Geotechnical Journal*, 59(3), 330-341. http://doi.org/10.1139/cgj-2020-0757.

Marsh, T., Kirby, C., Muchan, K., Barker, L., Henderson, E., & Hannaford, J. (2016). *The winter floods of 2015/2016 in the UK: a review.* London: National Hydrological Monitoring Programme. Retrieved in May 4, 2025, from http://nora.nerc.ac.uk/515303/1/N515303CR.pdf

McGeown, C., Hester, D., O'Brien, E.J., Kim, C.-W., Fitzgerald, P., & Pakrashi, V. (2024). Condition monitoring of railway bridges using vehicle pitch to detect scour. *Sensors*, 24(5), 1684. http://doi.org/10.3390/s24051684.

Moldovan, I.D., & Gomes Correia, A. (2017). Fixed point automatic interpretation of bender-based G0 measurements. *Computers and Geotechnics*, 89, 128-142. http://doi.org/10.1016/j.compgeo.2017.04.016.

Moldovan, I.D., & Gomes Correia, A. (2021). Optimisation of receiver's location in bender element experiments using computational wave filtration. *Soil Dynamics and Earthquake Engineering*, 143, 106591.

Moldovan, I.D., Climent, N., Bendea, E.D., Cismasiu, I., & Gomes Correia, A. (2021). A hybrid-Trefftz finite element platform for solid and porous elastodynamics. *Engineering Analysis with Boundary Elements*, 124, 155-173.

Moldovan, I.D., Almukashfi, A., & Gomes Correia, A. (2024). A computational platform for automatic signal processing for bender element sensors. *Algorithms*, 17(4), 131. http://doi.org/10.3390/a17040131.

Moldovan, I.D., Roshan, M.J., Azenha, M., & Gomes Correia, A. (2025). Dissipation boundaries for bender element experiments on geomaterials based on experimental and computational models. *Transportation Engineering*, 20, 100331. http://doi.org/10.1016/j.treng.2025.100331.

Nhu, V.-H., Mohammadi, A., Shahabi, H., Ahmad, B.B., Al-Ansari, N., Shirzadi, A., Geertsema, M., Kress, R., Karimzadeh, V., Valizadeh, S., Kamran, K., Chen, W., & Nguyen, H. (2020). Landslide Detection and Susceptibility Modeling on Cameron Highlands (Malaysia): a comparison between Random Forest, Logistic Regression and Logistic Model Tree Algorithms. *Forests*, 11(8), 830. http://doi.org/10.3390/f11080830.

Nikmehr, B., Hosseini, M.R., Wang, J., Chileshe, N., & Rameezdeen, R. (2021). BIM-based tools for managing Construction and Demolition Waste (CDW): a scoping review. *Sustainability*, 13(15), 8427. http://doi.org/10.3390/su13158427.

O'Donovan, J., O'Sullivan, C., Marketos, G., & Muir Wood, D. (2015). Analysis of bender element test interpretation using the discrete element method. *Granular Matter*, 17(2), 197-216. http://doi.org/10.1007/s10035-015-0552-6.

O'Brien, E.J., McCrum, D.P., Khan, M.A., & Prendergast, L.J. (2023). Wavelet-based operating deflection shapes for locating scour-related stiffness losses in multi-span bridges. *Structure and Infrastructure Engineering*, 19(2), 238-253. http://doi.org/10.1080/15732479.2021.1937235.

Owusu-Ansah, D., Tinoco, J., Matos, J., & Cabral, R. (2024). Combining slope satellite image analysis and artificial intelligence algorithms for highway service level assessment. In N. Guerra, M. M. Fernandes, C. Ferreira, A. Gomes Correia, A. Pinto & P.S. Pinto (Eds.), *Geotechnical engineering challenges to meet current and emerging needs of society* (pp. 1269-1272). London: CRC Press. http://doi.org/10.1201/9781003431749-230.

Pacheco-Torgal, F., Ding, Y., Colangelo, F., Tuladhar, R., & Koutamanis, A. (2020). *Advances in construction and demolition waste recycling.* Oxford: Elsevier.

Prendergast, L.J., Hester, D., & Gavin, K. (2016). Determining the presence of scour around bridge foundations using vehicle-induced vibrations. *Journal of Bridge Engineering*, 21(10), 04016065. http://doi.org/10.1061/(ASCE)BE.1943-5592.0000931.

Roshan, M.J., & Gomes Correia, A. (2025). Multifunctional cementitious composites from fabrication to their application in pavement: a comprehensive review. *Applied Sciences*, 15(7), 3451. http://doi.org/10.3390/app15073451.

Roshan, M.J., Rashid, A.S., Abdul Wahab, N., Tamassoki, S., Jusoh, S.N., Hezmi, M.A., Nik Daud, N.N., Mohd Apandi, N., & Azmi, M. (2022). Improved methods to prevent railway embankment failure and subgrade degradation: a review. *Transportation Geotechnics*, 37, 100834. http://doi.org/10.1016/j.trgeo.2022.100834.

Roshan, M.J., Abedi, M., Gomes Correia, A., & Fangueiro, R. (2023). Application of self-sensing cement-stabilized sand for damage detection. *Construction & Building Materials*, 403, 133080. http://doi.org/10.1016/j.conbuildmat.2023.133080.

Roshan, M.J., Abedi, M., Fangueiro, R., Gomes Correia, A., & Silva, M. M. (2024a). Evaluation procedure for damage detection by a self-sensing cement composite. *Measurement*, 226, 114149.

Roshan, M.J., Abedi, M., Gomes Correia, A., & Fangueiro, R. (2024b). Performance of self-sensing cement-stabilized sand under various loading conditions. *Sensors*, 24(6), 1737. http://doi.org/10.3390/s24061737.

Roshan, M.J., Abedi, M., Gomes Correia, A., Fangueiro, R., & Mendes, P.M. (2024c). A multifunctional cementitious composite for pavement subgrade. *Materials* , 17(3), 621. http://doi.org/10.3390/ma17030621.

Roshan, M., Bendea, D., Moldovan, I., Martins, M., Pultorak, M., Gomes Correia, A., & Azenha, M. (2024d). Impact of damping boundaries on the quality of the output signal in bender element experiments. In *Proceedings of the 7th International Conference on Geotechnical and Geophysical Site Characterization* (pp. 18-21), Barcelona. http://doi.org/10.23967/isc.2024.310.

Roshan, M.J., Gomes Correia, A., Fangueiro, R., & Mendes, P.M. (2025). Self-sensing cementitious composites for structural health monitoring: recent advances and challenges and future prospects. *Measurement Science & Technology*, 36(1), 012006. http://doi.org/10.1088/1361-6501/ad929a.

Sassani, A., Ceylan, H., Kim, S., Arabzadeh, A., Taylor, P.C., & Gopalakrishnan, K. (2018). Development of carbon fiber-modified electrically conductive concrete for implementation in Des Moines International Airport. *Case Studies in Construction Materials*, 8, 277-291. http://doi.org/10.1016/j.cscm.2018.02.003.

Selvakumaran, S., Plank, S., Geiß, C., Rossi, C., & Middleton, C. (2018). Remote monitoring to predict bridge scour failure using Interferometric Synthetic Aperture Radar (InSAR) stacking techniques. *International Journal of Applied Earth Observation and Geoinformation*, 73, 463-470. http://doi.org/10.1016/j.jag.2018.07.004.

Shirley, D.J., & Hampton, L.D. (1978). Shear-wave measurements in laboratory sediments. *The Journal of the Acoustical Society of America*, 63(2), 607-613. http://doi.org/10.1121/1.381760.

Shokravi, H., Vafaei, M., Samali, B., & Bakhary, N. (2024). In-fleet structural health monitoring of roadway bridges using connected and autonomous vehicles' data. *Computer-Aided Civil and Infrastructure Engineering*, 39(14), 2122-2139. http://doi.org/10.1111/mice.13180.

Standard, E. (2016). *Government ministers turn up to meet flooded villagers on the wrong side of a collapsed bridge.* London. Retrieved in April 27, 2025, from https://www.standard.co.uk/news/uk/government-ministers-turn-up-to-meet-flooded-villagers-on-the-wrong-side-of-a-collapsed-bridge-a3148481.html

Tawelian, L.R., & Mickovski, S.B. (2016). The implementation of geotechnical data into the BIM process. *Procedia Engineering*, 143(Ictg), 734-741. http://doi.org/10.1016/j.proeng.2016.06.115.

Tian, W., Zhang, Z., Qiu, R., Lu, J.-X., Li, R., Liu, Y., & Wang, W. (2024). Electrical performance of conductive cementitious composites under different curing regimes: enhanced conduction by carbon fibers towards self-sensing function. *Construction & Building Materials*, 421, 135771. http://doi.org/10.1016/j.conbuildmat.2024.135771.

Tola, S., Tinoco, J., Matos, J.C., & O'Brien, E. (2023a). Scour detection with monitoring methods and machine learning algorithms: a critical review. *Applied Sciences*, 13(3), 1661. http://doi.org/10.3390/app13031661.

Tola, S., Tinoco, J., Matos, J., & O'Brien, E. (2023b). Vulnerability assessment of existing bridges to scour, based on an indirect monitoring approach and machine learning tools. *Transportation Research Procedia*, 72, 751-758. http://doi.org/10.1016/j.trpro.2023.11.464.

Universidade Lusófona. (2023). *INTENT: intelligent health monitoring of road infrastructures using bender elements embedded in pavements.* Retrieved in May 4, 2025, from https://intent.ulusofona.pt/description

University of Minho. (2022). *RecycleBIM: integrated planning and recording circularity of construction materials through digital modelling.* Braga.

Venables, W.N., Smith, D.M., & Team, R.C. (2024). *An introduction to R*. London: Chapman & Hall/CRC. .

Viggiani, G., & Atkinson, J.H. (1995). Interpretation of bender element tests. *Geotechnique*, 45(1), 149-154. http://doi.org/10.1680/geot.1995.45.1.149.

Yamashita, S., Kawaguchi, T., Nakata, Y., Mikami, T., Fujiwara, T., & Shibuya, S. (2009). Interpretation of international parallel test on the measurement of G_{max} using bender elements. *Soil and Foundation*, 49(4), 631-650. http://doi.org/10.3208/sandf.49.631.

Zhang, J., Wu, C., Wang, Y., Ma, Y., Wu, Y., & Mao, X. (2018). The BIM-enabled geotechnical information management of a construction project. *Computing*, 100(1), 47-63. http://doi.org/10.1007/s00607-017-0571-8.

Zhang, T., Zhu, J., Xiong, Z., Zheng, K., & Wu, M. (2023). A new drive-by method for bridge damage inspection based on characteristic wavelet coefficient. *Buildings*, 13(2), 397. http://doi.org/10.3390/buildings13020397.